

1 **Development of East Asia Regional**
2 **Reanalysis based on advanced hybrid gain**
3 **data assimilation method and evaluation**
4 **with E3DVAR, ERA-5, and ERA-Interim**
5 **reanalysis**

6
7
8 Eun-Gyeong Yang, Hyun Mee Kim^{*}, and Dae-Hui Kim

9 *Atmospheric Predictability and Data Assimilation Laboratory*

10 *Department of Atmospheric Science, Yonsei University, Seoul, Republic of Korea*

11
12
13
14 Submitted to *Earth System Science Data*

15 June 28, 2021

16 Revision submitted on March 17, 2022

17

^{*} *Corresponding author address:* Hyun Mee Kim, Department of Atmospheric Sciences, Yonsei University, 50 Yonsei-ro, Seodaemun-gu, Seoul, 03722, Republic of Korea.

E-mail: khm@yonsei.ac.kr

18 **ABSTRACT**

19 The East Asia Regional Reanalysis (EARR) system is developed based on the advanced
20 hybrid gain data assimilation method (AdvHG) using Weather Research and Forecasting (WRF)
21 model and conventional observations. Based on EARR, the high-resolution regional reanalysis
22 and reforecast fields are produced with 12 km horizontal resolution over East Asia for 2010–
23 2019. The newly proposed AdvHG is based on the hybrid gain approach, weighting two
24 different analysis for an optimal analysis. The AdvHG is different from the hybrid gain in that
25 1) E3DVAR is used instead of EnKF, 2) 6 h forecast of ERA5 is used to be more consistent
26 with WRF, and 3) the pre-existing, state-of-the-art reanalysis is used. Thus, the AdvHG can be
27 regarded as an efficient approach to generate regional reanalysis dataset due to cost savings as
28 well as the use of the state-of-the-art reanalysis. The upper air variables of EARR are verified
29 with those of ERA5 for January and July 2017 and the ten-year period of 2010-2019. For upper
30 air variables, ERA5 outperforms EARR over two years, whereas EARR outperforms (shows
31 comparable performance to) ERA-I and E3DVAR for January in 2017 (July in 2017). EARR
32 better represents precipitation than ERA5 for January and July in 2017. Therefore, though the
33 uncertainties of upper air variables of EARR need to be considered when analyzing them, the
34 precipitation of EARR is more accurate than that of ERA5 for both two seasons. The EARR
35 data presented here can be downloaded from <https://doi.org/10.7910/DVN/7P8MZT> (Yang and
36 Kim 2021b) for data on pressure levels and <https://doi.org/10.7910/DVN/Q07VRC> (Yang and
37 Kim 2021c) for precipitation.

38

39 **1. Introduction**

40 Reanalysis datasets have been widely used in the socio-economical field as well as
41 meteorological and climate research areas all over the world. Most of reanalysis datasets
42 consist of global reanalysis whose spatial and temporal resolutions are relatively coarse (e.g.,
43 Schubert et al. 1993; Kalnay et al. 1996; Gibson et al. 1997; Kistler et al. 2001; Kanamitsu et
44 al. 2002; Uppala et al. 2005; Onogi et al. 2007; Bosilovich 2008; Saha et al. 2010; Dee et al.
45 2011; Rienecker et al. 2011; Bosilovich 2015; Kobayashi et al. 2015; Hersbach et al. 2020). As
46 the importance of regional reanalysis dataset emerged, many operational centers and research
47 institutes around the world have been producing the dataset in their own areas (Mesinger et al.
48 2006; Renshaw et al. 2013; Borsche et al. 2015; Bromwich et al. 2016; Jerney and Renshaw
49 2016; Zhang et al. 2017; Bromwich et al. 2018; Fukui et al. 2018; He et al. 2019; Ashrit et al.
50 2020).

51 The long-term high-resolution datasets are essential to investigate the past extreme
52 weather events which might be associated with mesoscale features such as heavy rainfall events
53 with high spatial and temporal variability which coarser-resolution model cannot represent.
54 The dynamical downscaling approaches can be a solution for generating high-resolution dataset,
55 but they have some issues with insufficient spin-up (Kayaba et al. 2016). Moreover, Fukui et
56 al. (2018) demonstrated that regional reanalysis over Japan assimilating only the conventional
57 observations had the potential to reproduce precipitation fields better than the dynamical
58 downscaling approaches. Ashrit et al. (2020) also found that the high-resolution regional
59 reanalysis over India showed substantial improvements of regional hydroclimatic features
60 during summer monsoon for the period of 1979-1993 compared to the global reanalysis ERA-
61 Interim (ERA-I, Dee et al. 2011) from ECMWF. Furthermore, He et al. (2019) revealed that
62 the pilot regional reanalysis over the Tibetan Plateau was able to represent more accurate

63 precipitation features as well as atmospheric humidity than the global reanalyses of ECMWF
64 (i.e., ECMWF's fifth-generation reanalysis (ERA5, Hersbach et al. 2020) and ERA-I).

65 As part of this effort, regional reanalysis over East Asia were produced based on the
66 Unified Model for the two-year period of 2013-2014 and it was confirmed that regional
67 reanalysis over East Asia is beneficial (Yang and Kim 2017; Yang and Kim 2019). However,
68 because UM was no longer available for generating regional reanalysis over East Asia, another
69 numerical weather prediction (NWP) model and its data assimilation (DA) method are required.

70 To find the most appropriate and cost-efficient DA method for a regional reanalysis over
71 East Asia, several DA methods were compared. Yang and Kim (2021) demonstrated that the
72 hybrid ensemble-variational data assimilation method (E3DVAR) shows the better
73 performance compared to three-dimensional variational data assimilation (3DVAR) and
74 ensemble Kalman filter (EnKF) over East Asia for January and July in 2016. However, it is
75 essential to confirm if this hybrid method is accurate enough to be used for a regional reanalysis
76 over East Asia. Thus, E3DVAR was compared with the latest and the previous reanalysis data
77 from ECMWF (ERA5 and ERA-I) for (re)analysis and (re)forecast variables and it was found
78 that a performance for a regional reanalysis needs to be further improved.

79 For this reason, a new advanced hybrid gain (AdvHG) data assimilation method, which
80 combines E3DVAR and ERA5 based on WRF model, is newly proposed and investigated in
81 this study. A hybrid gain data assimilation method has been developed as a new kind of hybrid
82 methods (Penny 2014). Based on this method, an advanced data assimilation method is newly
83 developed in this study. Finally, using this newly proposed DA method (AdvHG), East Asia
84 regional reanalysis (EARR) system is developed based on WRF model. EARR datasets have
85 been produced for ten-year period of 2010-2019 and are publicly available
86 (<https://dataverse.harvard.edu/dataverse/EARR>).

87 To investigate the accuracy and uncertainty of the state-of-the-art AdvHG DA algorithm

88 developed in this study, analysis and forecast atmospheric variables of E3DVAR, AdvHG,
89 WRF-based ERA-I, and WRF-based ERA5 are evaluated for January and July in 2017,
90 respectively. In addition, reforecast precipitation fields of ERA-I and ERA5 from ECMWF are
91 also verified and compared. In this study, the datasets are evaluated for two-month period
92 (January and July in 2017) or ten-year period (2010-2019) depending on the availability of
93 datasets. The reanalysis and (re)forecast fields of the EARR based on AdvHG and ERA5 are
94 verified for ten-year period (2010-2019). In section 2, the EARR system including model, data
95 assimilation method, and observations are explained. In section 3, the evaluation methods are
96 presented. The verification results of (re)analysis and (re)forecast variables are presented in
97 section 4. Section 4.1 presents evaluation results for wind, temperature, and humidity variables,
98 and section 4.2 presents those for precipitation (re)forecast. Section 5 presents data availability.
99 Lastly, summary and conclusions are presented in section 6.

100 **2. Reanalysis system**

101 *2.1. Model*

102 In this study, the Advanced Research Weather Research and Forecasting (WRF, v3.7.1)
103 model is used with 12-km horizontal resolution (540 x 432 grid points) and 50 vertical levels
104 (up to 5 hPa) for East Asia domain shown in Fig. 1. The model settings and physics scheme are
105 summarized in Table 1. Analysis fields are obtained every 6 h (00, 06, 12, and 18 UTC) via
106 assimilation of conventional observations with a 6 h assimilation window, and forecast fields
107 are integrated up to 36 h. The ERA5 reanalysis (Hersbach et al. 2020) is used as the first initial
108 condition before the cycling, and as boundary conditions every 6 h.

109 *2.2. Data assimilation methods*

110 *2.2.1. E3DVAR*

111 The E3DVAR method is one of hybrid data assimilation methods, which use a static

112 climatological background error covariance (BEC) and ensemble-based flow-dependent BEC,
 113 and couples the EnKF and 3DVAR (Zhang et al. 2013). E3DVAR is based on a cost function
 114 of 3DVAR. In E3DVAR, EnKF provides flow-dependent BEC as well as updates perturbations
 115 for ensemble members. Following Zhang et al. (2013),

$$J^b = J_s^b + J_e^b = \frac{1}{2} \delta \mathbf{x}^T \left[(1 - \beta) \mathbf{B} + \beta \mathbf{P}^f \circ \mathbf{C} \right]^{-1} \delta \mathbf{x} , \quad (1)$$

116 where J_s^b is a traditional cost function based on a static climatological BEC \mathbf{B} and J_e^b is an
 117 additional cost function based on ensemble-based BEC \mathbf{P}^f . \mathbf{C} is a correlation matrix for
 118 localization of the ensemble covariance \mathbf{P}^f . The weighting coefficient β between static and
 119 ensemble-based BEC is set to 0.8 in this study. To account for model error for E3DVAR, multi-
 120 physics scheme is applied to 40-member ensembles. Yang and Kim (2021) found that E3DVAR
 121 is the most appropriate DA method among 3DVAR, EnKF, and E3DVAR methods over East
 122 Asia. More detailed information on E3DVAR implemented in this study can be found in Yang
 123 and Kim (2021).

124 2.2.2. Hybrid gain data assimilation method

125 In the last decade, the traditional hybrid methods have been widely used for many
 126 operational centers and research institutes. Recently, Penny (2014) has proposed a new class
 127 of hybrid gain methods combining desirable aspects of both variational and EnKF families of
 128 algorithms by weighting analyses from 3DVAR and LETKF for an optimal analysis in the
 129 Lorenz 40-component model. Since then, this algorithm has been implemented at ECMWF
 130 (Bonavita et al. 2015) and at a hybrid global ocean DA system in National Centers for
 131 Environmental Prediction (NCEP) (Penny et al. 2015).

132 The hybrid gain algorithm can be described with the following equations:

$$\mathbf{x}_{Hyb}^a = \alpha \mathbf{x}_{det}^a + (1 - \alpha) \overline{\mathbf{x}^a} , \quad (2)$$

133 where \mathbf{x}_{Hyb}^a , \mathbf{x}_{det}^a , and $\overline{\mathbf{x}^a}$ denote the hybrid analysis, deterministic analysis, and the ensemble

134 mean analysis from the ensemble-based assimilation method, and α is a tunable parameter
 135 (Penny 2014, Houtekamer and Zhang 2016).

136 The hybrid gain method is different from traditional hybrid methods, in that a hybrid gain
 137 approach linearly combines analysis fields from EnKF and variational DA method to produce
 138 a hybrid gain analysis rather than linearly combining respective BECs (Penny 2014). Basically,
 139 the hybrid gain method is to hybridize two different Kalman gain matrices of ensemble-based
 140 [Eq. (4)] and variational data assimilation system [Eq. (5)] as in Eq. (3).

$$\hat{\mathbf{K}} = \beta_1 \mathbf{K}^f + \beta_2 \mathbf{K}^B + \beta_3 \mathbf{K}^B \mathbf{H} \mathbf{K}^f, \quad (3)$$

141 where

$$\mathbf{K}^f = \mathbf{P}^f \mathbf{H}^T (\mathbf{H} \mathbf{P}^f \mathbf{H}^T + \mathbf{R})^{-1}, \quad (4)$$

$$\mathbf{K}^B = \mathbf{B} \mathbf{H}^T (\mathbf{H} \mathbf{B} \mathbf{H}^T + \mathbf{R})^{-1}. \quad (5)$$

142 \mathbf{H} is an observation operator mapping the model state vector to observation space and \mathbf{R} is the
 143 observation error covariance matrix. The matrices \mathbf{P}^f and \mathbf{B} indicate the ensemble-based and
 144 the static climatological BEC, respectively. By choosing the specific coefficients ($\beta_1=1$, $\beta_2 =$
 145 α , $\beta_3 = -\alpha$), it can be written as in Eq. (6) and it can give an algebraically equivalent result
 146 with Eq. (2) (Penny 2014).

$$\hat{\mathbf{K}} = \mathbf{K}^f + \alpha \mathbf{K}^B (\mathbf{I} - \mathbf{H} \mathbf{K}^f). \quad (6)$$

147 One of advantages of the hybrid gain algorithm with respect to its development is that pre-
 148 existing operational systems can be used without significant modification for a hybrid analysis
 149 (Penny 2014) and independent parallel development of respective methods is allowed
 150 (Houtekamer and Zhang 2016). Furthermore, the hybrid gain approach can be considered as a
 151 practical and straightforward method in the foreseeable future to combine advantageous
 152 features of both ensemble- and variational-based DA algorithms (Houtekamer and Zhang 2016).

153 More detailed information on this algorithm can be found in Penny (2014).

154 2.2.3. *Advanced hybrid gain data assimilation method*

155 In this study, based on the hybrid gain approach, an advanced hybrid gain data assimilation
156 method (AdvHG) is newly proposed as follows:

$$X_{\text{AdvHG}}^a = \alpha X_{\text{ERA5}}^{f(6h)} + (1 - \alpha) \bar{X}_{\text{E3DVAR}}^a, \quad (7)$$

157 where $X_{\text{ERA5}}^{f(6h)}$ denotes the 6 h forecast of ERA5 reanalysis based on WRF model and $\bar{X}_{\text{E3DVAR}}^a$
158 denotes the analysis of E3DVAR (Fig. 2). In Eq. (7), α is a tunable parameter and is assigned
159 to be 0.5 in this study. This advanced hybrid gain approach is different from the hybrid gain
160 approach in that 1) E3DVAR analysis is used instead of EnKF, 2) 6 h forecast of ERA5 is used
161 instead of deterministic analysis from variational DA method, and 3) the pre-existing and state-
162 of-the-art reanalysis data (i.e., ERA5) is simply used instead of producing deterministic
163 analysis by assimilation. The reasons for these different approaches proposed in this study are
164 as follows:

165 1) E3DVAR is used instead of EnKF because Yang and Kim (2021) confirmed that
166 E3DVAR outperforms EnKF for winter and summer seasons over East Asia.

167 2) Instead of deterministic analysis, the 6 h forecast of ERA5 based on WRF model is
168 used to make the hybrid analysis more balanced and consistent with WRF model, because
169 ERA5 reanalysis fields are based on its own modeling system with coarser resolution, which
170 is different from that of this study.

171 3) European Centre for Medium-Range Weather Forecasts (ECMWF) reanalysis (ERA5)
172 is used instead of producing our own analysis fields from a variational DA method. This is a
173 very efficient approach because of the cost savings as well as the use of the high-quality latest
174 reanalysis from ECMWF assimilating all currently available observations with the state-of-the-
175 art and advanced technology.

176 Therefore, the approach proposed in this study is called as “advanced hybrid gain method”
177 (denoted as “AdvHG”).

178 2.3. Observations

179 The NCEP PrepBUFR [Prepared or QC’d data in BUFR (Binary Universal Form for the
180 Representation of meteorological data) format] conventional observations (global upper air and
181 surface weather observations, NCEP/NWS/NOAA/U.S.DOC 2008) are used every 6 h (00, 06,
182 12, and 18 UTC) for an assimilation by E3DVAR and AdvHG methods (Fig. 1). The PrepBUFR
183 is the output of the final process for preparing the observations to be assimilated in the different
184 NCEP analyses. For observations, rudimentary multi-platform quality control (QC) and more
185 complex platform-specific QC were conducted (e.g., surface pressure, rawinsonde heights and
186 temperature, wind profiler, aircraft wind and temperature) in NCEP (Keyser 2013).
187 Furthermore, if the innovations (i.e., observation minus background) of some observations are
188 greater than 5 times the observational error, then that observation is rejected during assimilation
189 procedure in this study.

190 The assimilated observations are as follows: the surface observations (SYNOP, METAR,
191 Ship, and Buoy), radiosonde observation (SOUND), upper-wind report (PILOT), wind profiler,
192 aircraft, atmospheric motion vector (AMV) wind from satellites, and Scatterometer oceanic
193 surface winds (Scatwind), and precipitable water vapor from global positioning system
194 (GPSPW). The observation errors depending on each observation platform, variable, and
195 vertical levels are assigned based on the default observation error statistics provided in
196 WRFDA system (Table 2). All observations are spatially thinned by 20 km except for AMV
197 thinned by 200 km as done by Warrick (2015), Cotton et al. (2016), and Shin et al. (2016).

198 To evaluate 6 h accumulated precipitation simulated by E3DVAR, AdvHG, ERA-I, and
199 ERA5 over East Asia, global surface weather observations (NCEP PrepBUFR,
200 NCEP/NWS/NOAA/U.S.DOC 2008) are used every 6 h (00, 06, 12, and 18 UTC). For an

201 evaluation of the monthly precipitation fields, the world monthly surface station climatology
202 (NCDC/NESDIS/NOAA/U.S.DOC et al. 1981) over 4700 different stations (2600 in more
203 recent years) is used.

204 *2.4. Global reanalysis datasets*

205 To compare EARR generated with other reanalysis datasets, ERA5 (Hersbach et al. 2020)
206 and ERA-I (Dee et al. 2011) reanalysis are chosen. The horizontal resolutions of ERA-I and
207 ERA5 are approximately 79 km (TL255) and 31 km (TL639), respectively. Because ERA5 is
208 based on the operational system in 2016, improvements in model physics, numerics, data
209 assimilation, and additional observations over the last decade are the advantages of ERA5
210 (Hersbach et al. 2018).

211 In this study, (re)forecast as well as reanalysis fields need to be verified. Regarding
212 reanalysis and (re)forecast fields of ECMWF, reanalysis fields (i.e., ERA5 and ERA-I)
213 downloaded from ECMWF are evaluated (Figs. 3 and 6). There are two different (re)forecast
214 fields (e.g., ERA5_fromECMWF, WRF-based ERA5) used in this study. WRF-based ERA5
215 and ERA-I are forecast fields based on WRF model with 12 km horizontal resolution where
216 ERA5 and ERA-I are used as initial conditions, respectively. In contrast, ERA5_fromECMWF
217 and ERA-I_fromECMWF are reforecast fields based on ECMWF model not WRF model, so
218 the reforecast fields of ERA5 and ERA-I are provided and downloaded from ECMWF. These
219 reforecast fields are only used for evaluation of precipitation (Figs. 8 and 9). The (re)analysis
220 and (re)forecast fields and corresponding experiments are explained in Table 3.

221 **3. Evaluation method**

222 *3.1. Equitable threat score and Frequency bias index*

223 Based on the contingency table (Table 4), ETS is defined as

$$\text{ETS} = \frac{A - A_r}{A + B + C - A_r}, \text{ where } A_r = \frac{(A + B)(A + C)}{A + B + C + D}. \quad (8)$$

224 The ETS range is from -1/3 to 1 and the value 1 for ETS is a perfect score. ETS is a more
 225 balanced score than Probability of Detection (POD) and False Alarm Ratio (FAR), because it
 226 is sensitive to both false alarms and misses (Wilson 2010).

227 FBI is defined as

$$\text{FBI} = \text{Bias} = \frac{A + B}{A + C}. \quad (9)$$

228 The FBI indicates whether the model tends to over-forecast (too frequently, $\text{FBI} > 1$) or under-
 229 forecast (not frequent enough, $\text{FBI} < 1$) events with respect to frequency of occurrence.

230 *3.2 Probability of detection and False alarm ratio*

231 Based on the contingency table (Table 4), POD is defined as

$$\text{POD} = \frac{A}{A + C} = \frac{\text{Hits}}{\text{Hits} + \text{Misses}}. \quad (10)$$

232 The POD range is from 0 to 1. POD is required to be used with FAR, because POD can be
 233 artificially improved by systematically over-forecasting the events (Wilson 2010).

234 FAR is defined as

$$\text{FAR} = \frac{B}{A + B} = \frac{\text{False alarms}}{\text{Hits} + \text{False alarms}}. \quad (11)$$

235 The range of FAR is from 0 to 1 and its lower score implies a higher accuracy.

236 *3.3 Brier skill score*

237 Verification of the performance of high-resolution forecast with the traditional verification
 238 metrics (e.g., ETS, FBI) can be misleading due to double penalty, particularly for highly
 239 variable fields (e.g., precipitation). Therefore, as one of spatial verification approaches that do
 240 not require forecast to match point observation spatially, neighborhood (fuzzy) verification
 241 method, which assumes that slightly displaced forecast can be acceptable and a local

242 neighborhood can define the degree of allowable displacement (Ebert 2008; Kim et al. 2015;
 243 On et al. 2018), is used in this section. According to Ebert (2008), depending on the matching
 244 strategy, neighborhood verifications can be categorized into two frameworks: ‘single
 245 observation-neighborhood forecast (SO-NF)’ where neighborhood forecasts surrounding
 246 observations are considered, and ‘neighborhood observation-neighborhood forecast (NO-NF)’
 247 strategies where not only neighborhood forecasts but also neighborhood observations
 248 surrounding observations are considered. Due to the absence of high-resolution gridded
 249 precipitation observation data in East Asia, various verification scores widely used as
 250 ‘neighborhood observation-neighborhood forecast (NO-NF)’ strategy are not available in this
 251 study. Thus, in this section, Brier skill score as one of ‘single observation-neighborhood
 252 forecast (SO-NF)’ strategy is introduced.

253 The Brier score (BS) is similar to the mean-squared error (MSE) and is defined as (Wilks
 254 2006):

$$BS = \frac{1}{N} \sum_{i=1}^N (p_i - o_i)^2. \quad (12)$$

255 where p_i denotes the probability forecast, and o_i denotes the binary observation which is either
 256 0 or 1, and N is the total number of observations during the given period. Generally, Brier skill
 257 score (or Brier score) is used to verify ensemble forecasts which are able to calculate
 258 probabilistic forecasts (Kay et al. 2013; Kim and Kim 2017). However, Brier skill score can
 259 also be used for deterministic forecasts using a pragmatic post-processing procedure (Theis et
 260 al., 2005; Mittermaier 2014), which derives probabilistic forecasts from deterministic forecasts
 261 at every model grid point by considering neighborhood forecast as *pseudo ensemble*.

$$BSS = 1 - \frac{BS}{BS_{\text{ref}}}, \quad (13)$$

262 where BS_{ref} is Brier score of reference. Brier skill score is skill score with respect to Brier score

263 as in Eq. (13). For reference, a climatology or other forecast can be used either. In this study,
 264 the WRF-based ERA-I is considered as a reference.

265 3.4 Pattern correlation coefficient

266 The pattern correlation coefficient (PCC) is defined as Eq. (14) (Shiferaw et al. 2018; Yoo
 267 and Cho 2018; Park and Kim 2020).

$$\text{PCC} = \frac{\sum_{i=1}^N (x_i - \bar{x})(o_i - \bar{o})}{\left[\sum_{i=1}^N (x_i - \bar{x})^2 \sum_{i=1}^N (o_i - \bar{o})^2 \right]^{1/2}}, \quad (14)$$

268 where x_i and o_i are (re)forecast and observed precipitation at i th observation location and the
 269 over-bar indicates the averaged variables over N observed stations in the verification area.

270 4. Results

271 4.1 Evaluation of wind, temperature, and humidity variables

272 4.1.1 RMSE for January and July 2017

273 The analysis and forecast RMSEs of E3DVAR, AdvHG, the WRF-based ERA-I, and
 274 WRF-based ERA5 are calculated for zonal wind, meridional wind, temperature, and Qvapor
 275 (water vapor mixing ratio in WRF) variables against sonde observations at 00 and 12 UTC in
 276 verification domain (dashed box in Fig. 1) for January and July in 2017 and averaged over each
 277 month (Figs. 3, 4, and 5).

278 For analysis RMSE (Fig. 3), E3DVAR is smaller than AdvHG for all pressure levels and
 279 variables, except for temperature in July at 1000 hPa and Qvapor in January and July at 1000
 280 hPa. In general, the analysis RMSE of AdvHG for all variables is comparable to or greater than
 281 that of ERA5. The analysis RMSE of ERA5 is smaller than that of ERA-I for all levels and
 282 variables; in particular, the analysis RMSE difference between ERA5 and ERA-I is distinctive
 283 for wind.

284 Regarding wind variables of analysis (Figs. 3a, b, c, and d), E3DVAR is the most closely
285 fitted to observations except for the wind in upper troposphere in January, followed by ERA5,
286 AdvHG, and ERA-I. For temperature RMSE (Figs. 3e and f), E3DVAR is smaller than AdvHG.
287 For Qvapor, RMSE in July is much larger than that in January due to a monsoonal flow carrying
288 moist air to East Asia. In general, Qvapor RMSE of E3DVAR is the smallest, followed by
289 ERA5, AdvHG, and ERA-I. Therefore, for all variables, generally E3DVAR analysis fields are
290 the most closely fitted to observations. Since the analysis RMSE implies how much analysis
291 fields are fitted to observations rather than the accuracy of analysis itself, not only analysis
292 RMSE but also forecast RMSE should be considered.

293 For 24 h forecast fields in January (Figs. 4a, c, e, and g), overall, RMSEs of AdvHG and
294 E3DVAR are greater than those of ERA5 and smaller than those of ERA-I, and AdvHG RMSE
295 is smaller than E3DVAR RMSE for all levels and variables. Meanwhile, for July (Figs. 4b, d,
296 f, and h), AdvHG and E3DVAR show comparable RMSE to ERA-I.

297 Furthermore, general features of 36 h forecast RMSE (Fig. 5) are similar to the 24 h
298 forecast RMSE (Fig. 4). However, particularly in January, the 36 h forecast RMSE differences
299 between ERA5 and ERA-I are more distinctive compared to those of 24 h forecast. In January,
300 the vertically averaged 36 h forecast RMSE differences of ERA5 and ERA-I are 0.52 m s^{-1} for
301 wind, 0.16 K for temperature, and 0.08 g kg^{-1} for Qvapor, whereas those of 24 h forecast are
302 0.4 m s^{-1} for wind, 0.11 K for temperature, and 0.06 g kg^{-1} for Qvapor. In addition, the 36 h
303 forecast RMSE differences between ERA5 and AdvHG for January are on average 0.1 m s^{-1}
304 for wind, 0.05 K for temperature, and 0.02 g kg^{-1} for Qvapor, which are even smaller compared
305 to those of 24 h forecast, implying that AdvHG is a lot more accurate than ERA-I for January
306 in 2017. For July, 36 h forecast RMSE of ERA5 is the smallest and RMSEs of AdvHG and
307 E3DVAR are similar to those of ERA-I.

308 *4.1.2 RMSE and spread for the period of 2010-2019*

309 In this section, EARR produced in this study is verified for a longer period with WRF-
310 based ERA5. RMSE and spread of reanalyses and reforecasts based on AdvHG method are
311 calculated and averaged over the period of 2010-2019. The reanalyses and (re)forecast fields
312 are evaluated by calculating RMSE valid at 00 and 12 UTC and spread at 00, 06, 12, and 18
313 UTC.

314 The averaged RMSEs of reanalysis for ERA5 and EARR (denoted as AdvHG in Fig. 6)
315 and spread of analysis and 6 h forecast fields of EARR (AdvHG) are shown in Fig. 6. With
316 respect to spread, the ensemble spreads of analysis fields are smaller than those of 6 h forecast
317 fields, on average, by 0.15 m s^{-1} for wind, 0.04 K for temperature, and 0.02 g kg^{-1} for Qvapor,
318 which is the well-known characteristics of ensemble-based data assimilation methods. To be
319 specific, the wind spread (Figs. 6a and b) is similar to or greater than the wind RMSE except
320 for the upper troposphere above 200 hPa, implying ensemble spread for wind is well
321 represented below 200 hPa. On the contrary, the ensembles for temperature and Qvapor (Figs.
322 6c and d) are underdispersive compared to their RMSEs.

323 Regarding reanalysis RMSE, overall AdvHG RMSE is greater than ERA5 RMSE for all
324 variables (Fig. 6). The vertically averaged RMSEs of AdvHG are greater by 0.16 m s^{-1} for wind,
325 0.09 K for temperature, and 0.01 g kg^{-1} for Qvapor than those of ERA5. Nonetheless, the wind
326 RMSEs of AdvHG are similar to those of ERA5 for the middle of troposphere (400–850 hPa),
327 and the Qvapor RMSEs of AdvHG are similar to those of ERA5 except for 1000 hPa.

328 In addition, regarding 24 h forecast RMSE, AdvHG shows larger RMSE than ERA5 for
329 all variables (Fig. 7). The vertically-averaged RMSE differences of wind, temperature, and
330 Qvapor variables between AdvHG and ERA5 are approximately 0.2 m s^{-1} , 0.07 K , and 0.03 g
331 kg^{-1} , respectively. These differences are smaller, compared to the 24 h forecast RMSE
332 difference between ERA-I and ERA5 shown in Fig. 4 (i.e., wind, temperature, and Qvapor
333 RMSE difference: 0.4 m s^{-1} , 0.11 K , and 0.06 g kg^{-1} for January 2017, 0.25 m s^{-1} , 0.05 K , and

334 0.04 g kg⁻¹ for July 2017).

335 4.2 Evaluation of precipitation for January and July in 2017.

336 4.2.1 Evaluation metrics

337 4.2.1.1 Equitable threat score and Frequency bias index

338 In this section, for the point-based Equitable threat score (ETS) and Frequency bias index
339 (FBI) based on Table 4, the 6 h accumulated precipitation fields based on the 6 h forecast of
340 E3DVAR, AdvHG, WRF-based ERA-I, WRF-based ERA5, ERA-I_fromECMWF, and
341 ERA5_fromECMWF are evaluated every 6 h (00, 06, 12, and 18 UTC) for January and July in
342 2017 (Fig. 8). Here, all the WRF-based precipitation fields are based on 12-km horizontal
343 resolution, and ERA-I_fromECMWF and ERA5_fromECMWF have 79- and 31-km horizontal
344 resolutions, respectively. Generally, ETS decreases as a threshold increases for both two
345 months (Figs. 8a and c). For January in 2017 (Fig. 8a), AdvHG ETS is the greatest among
346 others. Compared to precipitation reforecasts from ECMWF (i.e., ERA-I_fromECMWF,
347 ERA5_fromECMWF), AdvHG shows the higher ETS, indicating that AdvHG is able to
348 simulate more accurate precipitation fields than ERA-I and ERA5 from ECMWF in January
349 2017. Surprisingly, ETS of ERA5_fromECMWF for January in 2017 is the lowest among all
350 the results compared and is even lower than that of ERA-I_fromECMWF.

351 Since the precipitation reforecasts from ECMWF have not only coarser resolutions but
352 also different forecast model (i.e., the forecasting system of ECMWF), the precipitation
353 forecasts of ERA5 and ERA-I are additionally produced by using the same forecast model with
354 the same resolution as AdvHG and E3DVAR in this study, as explained in section 2.4. For
355 January 2017 (Fig. 8a), ETS of ERA5 (i.e., WRF-based ERA5) is higher than that of
356 ERA5_fromECMWF for all thresholds, whereas ETS of ERA-I (i.e., WRF-based ERA-I) is
357 lower than that of ERA-I_fromECMWF except for high thresholds (8 and 16 mm (6 h)⁻¹). The
358 ERA5 ETS is greater than the ERA-I ETS, but is smaller than the AdvHG ETS. The AdvHG

359 shows the greatest ETS among others with the same resolution and forecast model, and
360 E3DVAR, ERA5, and ERA-I follow.

361 Regarding FBI in winter (Fig. 8b), for 4, 8, and 16 mm (6 h)⁻¹ thresholds, all the results
362 show the FBI smaller than 1, implying the underestimation of frequency of precipitation for
363 high-threshold events. In general, AdvHG shows the FBI closest to 1 among all the results,
364 which is consistent with the greatest ETS of AdvHG. The E3DVAR FBI is similar to the
365 AdvHG FBI, and ERA5 and ERA-I FBIs are similar to each other.

366 Meanwhile, overall, the ETS values for January whose maximum is around 0.4 (Fig. 8a)
367 are much greater than those for July in 2017 whose maximum is around 0.2 (Fig. 8c), implying
368 that the precipitation forecast in summer is more difficult than that in winter. The ETS
369 difference between the results in July is smaller than those in January. Particularly, for the
370 thresholds 4 and 8 mm (6 h)⁻¹, ETSs in July are similar to each other (Fig. 8c). Except for those
371 two thresholds, the ETS of ERA-I_fromECMWF is the smallest. At the threshold 16 mm (6 h)
372 ⁻¹, ERA5 ETS is the highest, followed by AdvHG, E3DVAR, ERA-I, ERA5_fromECMWF, and
373 ERA-I_fromECMWF. At the threshold 0.5 and 1 mm (6 h)⁻¹, the E3DVAR ETS is the greatest,
374 followed by ERA5, AdvHG, ERA5_fromECMWF, ERA-I, and ERA-I_fromECMWF.

375 With respect to FBI in July 2017, the WRF-based results show the FBIs greater than 1,
376 whereas reforecast from ECMWF show the FBIs greater than 1 for 0.5, 1, and 4 mm (6 h)⁻¹
377 thresholds and smaller than 1 for higher thresholds (8 and 16 mm (6 h)⁻¹) (Fig. 8d). For July in
378 2017, in general, ERA5_fromECMWF FBI is the closest to 1, followed by E3DVAR, AdvHG,
379 ERA5, ERA-I, and ERA-I_fromECMWF FBI.

380 *4.2.1.2 Probability of detection and False alarm ratio*

381 The Probability of Detection (POD or Hit Rate) and False Alarm Ratio (FAR) are
382 calculated for precipitation simulated from E3DVAR, AdvHG, WRF-based ERA-I, WRF-
383 based ERA5, ERA-I_fromECMWF, and ERA5_fromECMWF for January and July in 2017

384 (Fig. 9). For January in 2017, AdvHG POD is the greatest among the WRF-based results,
385 followed by E3DVAR, ERA5, and ERA-I (Fig. 9a). In addition to the lowest ETS of
386 ERA5_fromECMWF for January in 2017 as discussed in the section 4.2.1.1, FAR of
387 ERA5_fromECMWF is extremely high with low POD in winter. Therefore, especially for
388 January in 2017, the precipitation fields simulated from EARR (AdvHG) over East Asia are a
389 lot more accurate than those from ERA5_fromECMWF.

390 For July in 2017, generally, AdvHG shows the largest POD, except for ERA5 (Fig. 9c).
391 With respect to FAR, FAR values in July are much greater than those in January, which is
392 consistent with the ETS difference between these two seasons.

393 *4.2.1.3 Brier skill score*

394 The neighborhood sizes are chosen to be $3\Delta x$, $5\Delta x$, $9\Delta x$, and $11\Delta x$, which are 36, 60,
395 108, and 132 km, respectively, and the thresholds 0.5, 1, 4, 8, and 16 mm (6 h)⁻¹ are considered.
396 The probabilistic precipitation forecasts are calculated at every model grid point depending on
397 neighborhood sizes and thresholds. Regarding each observation, the nearest model grid point
398 to observations is considered as the center of neighborhood. For verification, 6 h accumulated
399 precipitation fields are extracted from the first 0–6 h forecast fields of WRF-based ERA-I,
400 WRF-based ERA5, E3DVAR, and AdvHG every 6 h (00, 06, 12, and 18 UTC). BSSs of
401 ERA5_fromECMWF and ERA-I_fromECMWF are not calculated, because they have different
402 resolution from WRF-based results.

403 Based on the neighborhood approach, Brier skill score (BSS) is calculated depending on
404 different neighborhood sizes for January and July in 2017, respectively (Fig. 10). Because the
405 reference of Brier score is chosen as the ERA-I, the positive BSS implies better accuracy than
406 ERA-I. In general, for both two months, AdvHG BSS is greater than ERA5 BSS. Although the
407 E3DVAR BSS is the greatest in July 2017, the AdvHG BSS is the greatest in January 2017.

408 For January in 2017, as a neighborhood size increases, AdvHG and E3DVAR BSSs tend

409 to increase except for ERA5. Overall, AdvHG BSS is the greatest among other BSSs for all
410 thresholds for all neighborhood sizes. The ERA5 BSS is greater than E3DVAR BSS except for
411 16 mm (6 h)⁻¹. The highest BSS of AdvHG and the lowest BSS of ERA-I are consistent with
412 ETS result. Unlike greater E3DVAR ETS than ERA5 ETS, ERA5 BSS is greater than E3DVAR
413 BSS in January 2017.

414 For July 2017, while the ETS difference between the WRF-based results is not distinct
415 (Fig. 8c), the BSS difference is rather noticeable. Generally, E3DVAR BSS is the greatest
416 among other BSSs for all thresholds except for 16 mm (6 h)⁻¹ for neighborhood sizes 9 and 11.
417 Although E3DVAR BSS is the largest, AdvHG outperforms ERA5 and ERA-I. The worst
418 performance of ERA-I precipitation is consistent with ETS result. At 0.5, 1, and 4 mm (6 h)⁻¹
419 thresholds, E3DVAR BSS is the greatest, which is similar to ETS. At 8 and 16 mm (6 h)⁻¹
420 thresholds, ERA5 ETS is the highest, followed by AdvHG and E3DVAR, whereas overall
421 E3DVAR BSS is the highest, followed by AdvHG and ERA5.

422 4.2.2 *Spatial distribution*

423 4.2.2.1 *6 h accumulated precipitation with the pattern correlation coefficient*

424 In this section, the spatial distributions of 6 h accumulated precipitation from the WRF-
425 based forecast and reforecast from ECMWF are compared. In addition, pattern correlation
426 coefficients (PCC) are calculated and shown at the bottom right of Figs. 11 and 12.

427 The PCC is computed according to the usual Pearson correlation operating on the N
428 observed point pairs of 6 h accumulated precipitation fields simulated from (re)forecast and
429 observations at the specific time. For the calculation of PCC, 6 h accumulated precipitation
430 fields from (re)forecast fields are interpolated bilinearly to the N observed points.

431 Firstly, on 29th and 30th of January in 2017 (Fig. 11), it is noticeable that the precipitation
432 fields of AdvHG match observations well over East Asia, whereas, in particular, those of
433 ERA5_fromECMWF do not. For example, ERA5_fromECMWF overestimates precipitation

434 over inland area of China (Fig. 11zz), while AdvHG simulates precipitation similar to
435 observations regarding its position and intensity (Fig. 11x). ERA5_fromECMWF also shows
436 noticeably smaller PCC (Figs. 11g, n, and zz). Although PCC does not represent the exact
437 accuracy or predictability of precipitation, the overall feature of PCC is consistent with the
438 results found so far. For January in 2017, the averaged PCC of AdvHG is the greatest (i.e., 0.61)
439 and that of ERA5_fromECMWF is the smallest (i.e., 0.46) (not shown).

440 For 1st and 2nd of July in 2017 (Fig. 12), in general, AdvHG, E3DVAR, and ERA5 well
441 simulate not only overall features of precipitation fields but also their intensity. During July in
442 2017, ERA5 and ERA-I simulate heavier precipitation than AdvHG (not shown), which is
443 consistent with larger FBI of ERA5 and ERA-I at higher thresholds. For one-month period of
444 July in 2017, the averaged PCC of ERA5 is the greatest (i.e., 0.37) and that of AdvHG is 0.34,
445 but the PCC difference between ERA5 and AdvHG is not distinctive. Moreover, the overall
446 range of averaged PCC of different datasets in summer (i.e., 0.29-0.35) is smaller than that in
447 winter (i.e., 0.46-0.61), which is consistent with the seasonal difference of ETS in this study.

448 4.2.2.2 *Monthly accumulated precipitation*

449 In this section, the monthly accumulated precipitation fields of rain gauge based
450 observations, E3DVAR, AdvHG, ERA-I, ERA5, ERA-I_fromECMWF, and
451 ERA5_fromECMWF are compared to each other for two one-month periods in January and
452 July in 2017, respectively.

453 The monthly accumulated precipitation fields simulated by E3DVAR and AdvHG (Figs.
454 13b and c) are similar to each other, and E3DVAR and AdvHG produce the best fit to observed
455 fields. Especially, for the north-western part of Japan (e.g., Chugoku and Kinki), E3DVAR and
456 AdvHG are able to represent precipitation correctly, whereas ERA-I_fromECMWF and
457 ERA5_fromECMWF fail to do so (Fig. 13). Moreover, although all the results similarly
458 represent overall features of precipitation in January (Fig. 13), ERA5_fromECMWF (Fig. 13g)

459 simulates the overestimated precipitation over South China, which is consistent with the results
460 in the previous section as well as its larger FBI at lower thresholds (0.5 and 1 mm (6 h)^{-1}) shown
461 in Fig. 8b. It is noticeable that all results fail to represent the observed precipitation area over
462 Tibetan Plateau (25° – 40° N, 95° – 105° E).

463 For the monthly accumulated precipitation in July 2017, overall, the ERA5_fromECMWF
464 (Fig. 14g) and the WRF-based results (Figs. 14b, c, and e) except for ERA-I (Fig. 14d) well
465 simulate precipitation similar to observations. The WRF-based results including AdvHG
466 overestimate precipitation over western and southern part of Japan, while ERA-
467 I_fromECMWF and ERA5_fromECMWF simulate similar precipitation fields to observed
468 fields. The WRF-based results tend to overestimate precipitation in South China, Korea, and
469 Japan, compared to ERA-I_fromECMWF and ERA5_fromECMWF. This is consistent with
470 the result in Fig. 8d, in which FBIs from WRF-based results are generally greater than for
471 higher thresholds (8 and 16 mm (6 h)^{-1}), whereas those from ECMWF are smaller than 1.

472 Even though detailed precipitation features of WRF-based results are different, overall
473 features of precipitation from WRF-based results are similar to each other, which implies that
474 predictability of precipitation strongly depends on the physics schemes as well as NWP model,
475 especially for summer season. According to Que et al. (2016), depending on the combinations
476 of physics options in WRF model, the spatial distribution of precipitation can be significantly
477 different over Asian summer monsoon area and YSU PBL scheme which is used in this study
478 tends to overestimate precipitation over the same area. Thus, different physics options could
479 simulate the different spatial distribution of precipitation.

480 In addition, compared to ERA5 based on WRF model (Fig. 14e), ECMWF model for
481 ERA5_fromECMWF (Fig. 14g) seems to suppress precipitation. Thus, WRF model with the
482 physics schemes used in this study might simulate more precipitation than ECMWF model,
483 although the initial condition is the same. Therefore, it is important to consider the consistency

484 of the systems for data assimilation and forecast model for a good performance of forecast
485 weather variables like precipitation.

486 **5. Data Availability**

487 The EARR data presented in this study are available every 6 h (i.e., 00, 06, 12, and 18
488 UTC) for the period of 2010-2019 from Harvard Dataverse Repository
489 (<https://dataverse.harvard.edu/dataverse/EARR>). The EARR 6 hourly data on pressure levels
490 (<https://doi.org/10.7910/DVN/7P8MZT>, Yang and Kim 2021b) and 6 hourly precipitation data
491 (<https://doi.org/10.7910/DVN/Q07VRC>, Yang and Kim 2021c) are provided in NetCDF file
492 format.

493 The EARR 6 hourly data on pressure levels (Yang and Kim 2021b) include u-component
494 of wind, v-component of wind, temperature, geopotential height, and specific humidity
495 variables of reanalysis on pressure levels (i.e., 925, 850, 700, 500, 300, 200, 100, and 50 hPa).
496 The EARR 6 hourly precipitation data (Yang and Kim 2021c) contain 6 h accumulated total
497 precipitation variable of 6 h reforecast on single level. The 6 h accumulated total precipitation
498 is obtained from 6 h reforecast field which is integrated for 6 h from reanalysis field every 6 h
499 (i.e., 00, 06, 12 and 18 UTC).

500 **6. Summary and conclusions**

501 In this study, to develop the regional reanalysis system over East Asia, the advanced
502 hybrid gain algorithm (AdvHG) is newly proposed and evaluated with traditional hybrid DA
503 method (E3DVAR) as well as existing reanalyses from ECMWF (ERA5 and ERA-I) for
504 January and July in 2017. The East Asia Regional Reanalysis (EARR) system is developed
505 based on the AdvHG as the data assimilation method using WRF model and conventional
506 observations. The high-resolution regional reanalysis and reforecast fields over East Asia with
507 12 km horizontal resolution are produced and evaluated against observations with ERA5 for

508 the ten-year period of 2010–2019.

509 The AdvHG newly proposed in this study is based on the hybrid gain approach, weighting
510 analyses from variational-based and ensemble-based DA algorithms to generate optimal hybrid
511 analysis, which can play an important role as a simple and practical method in the foreseeable
512 future to take advantage of each strength of two different DA methods. The advanced hybrid
513 gain method is different from the hybrid gain approach in that 1) E3DVAR is used instead of
514 EnKF, 2) 6 h forecast of ERA5 is used instead of deterministic analysis for a more balanced
515 and consistent analysis with WRF model, and 3) the pre-existing and state-of-the-art reanalysis
516 data (i.e. ERA5) is simply used instead of producing our own analysis fields from a variational
517 DA method. Thus, it can be regarded as an efficient approach to generate regional reanalysis
518 dataset because of cost savings as well as the use of the state-of-the-art reanalysis from
519 ECMWF that assimilates all available observations.

520 For a verification, the latest ECMWF reanalysis and reforecast datasets (i.e., ERA5 and
521 ERA-I) are used. With respect to forecast variables, two different forecast fields of ECWTF
522 are used: 1) reforecast fields from ECMWF (i.e., ERA5_fromECMWF and ERA-
523 I_fromECMWF) and 2) forecast fields (i.e., WRF-based ERA5 and WRF-based ERA-I)
524 integrated in WRF model with 12 km resolution using ERA5 and ERA-I as initial conditions.

525 Analysis and forecast wind, temperature, and humidity variables of AdvHG are evaluated
526 with ERA5 for the ten-year period and evaluated with five different experiments (i.e., E3DVAR,
527 ERA5, ERA-I, ERA5_fromECMWF, ERA-I_fromECMWF) for January and July in 2017.
528 Overall, the analysis RMSE of E3DVAR is the smallest among others but comparable to that
529 of ERA5, especially for January in 2017. Regarding forecast variables, AdvHG outperforms
530 E3DVAR for January and July in 2017. Although ERA5 outperforms AdvHG for upper air
531 variables for two seasons in 2017, AdvHG outperforms ERA-I in January and shows
532 comparable performance to ERA-I in July. Additionally the verification results of AdvHG and

533 ERA5 for the period of 2010-2019 are consistent with those for two one-month period in 2017.

534 The precipitation forecast variables are also verified regarding a neighborhood-based
535 verification score (i.e., Brier skill score) as well as the point-based verification scores (i.e., ETS,
536 FBI, POD, and FAR). According to the point-based verification scores, the precipitation
537 forecast of AdvHG in January is the most accurate, followed by E3DVAR, ERA5, ERA-I. For
538 July, overall ETS values of all results are relatively lower compared to those in January,
539 implying the lower predictability in summer season. In addition, the ETS differences between
540 the results are not distinctive in July. For higher thresholds (8 and 16 mm (6 h)⁻¹) in July,
541 AdvHG ETS is greater than E3DVAR ETS and smaller than ERA5 ETS, whereas E3DVAR
542 ETS is the greatest followed by ERA5 and AdvHG for lower thresholds (0.5 and 1 mm (6 h)⁻¹).
543 ¹).

544 To prevent from double penalty when verifying a highly variable data with high resolution
545 (e.g., precipitation), Brier skill score (BSS) based on neighborhood approach is calculated for
546 6 h accumulated precipitation forecasts depending on different neighborhood sizes for January
547 and July in 2017. In general, BSS of AdvHG is greater than that of ERA5 and ERA-I for both
548 two months. Although the E3DVAR BSS is the greatest in July 2017, the AdvHG BSS is the
549 greatest in January 2017.

550 Lastly, the spatial distributions of 6 h and monthly accumulated precipitation forecast for
551 AdvHG, E3DVAR, ERA-I, ERA5, ERA-I_fromECMWF, and ERA5_fromECMWF are
552 compared with rain-gauge based observations. For January 2017, it is noticeable that AdvHG
553 precipitation is the closest to observations with highest PCC (i.e., 0.61) and
554 ERA5_fromECMWF overestimates precipitation over South China with the lowest PCC (i.e.,
555 0.46). For July in 2017, the WRF-based results tend to overestimate precipitation compared to
556 ERA-I_fromECMWF and ERA5_fromECMWF. In addition, even though the averaged PCC
557 of ERA5 (i.e., 0.37) is slightly greater than that of AdvHG (i.e., 0.34), the PCC difference

558 between ERA5 and AdvHG is not distinctive and overall range of averaged PCC of all datasets
559 in summer (i.e., 0.29-0.37) is smaller than that in winter (i.e., 0.46-0.6).

560 In conclusion, for upper air variables, overall, ERA5 outperforms EARR based on AdvHG,
561 but the RMSE difference between ERA5 and EARR (AdvHG) is smaller than that between
562 ERA5 and ERA-I. In addition, EARR outperforms ERA-I for January 2017 and shows
563 comparable performance to ERA-I for July 2017. On the contrary, according to the evaluation
564 results of precipitation, in general, EARR better represents precipitation than ERA5 as well as
565 ERA5_fromECMWF for January and July in 2017. Even if E3DVAR precipitation is better
566 represented than EARR precipitation for July, the difference is not considerable for July and
567 EARR better simulates precipitation for January than E3DVAR. Therefore, although the
568 uncertainties of upper air variables of EARR should be considered when analyzing them, the
569 precipitation reforecast of EARR is more accurate than that of ERA5 for both two seasons.

570 Combining the global reanalysis data (i.e., ERA5) characterized by the high quality of
571 large-scale features with detailed smaller-scale features in the higher resolution represented by
572 ensemble-based assimilation method (i.e., E3DVAR) as well as a community numerical
573 weather prediction model (i.e., WRF model) is a key factor of EARR to be able to produce
574 high-resolution initial conditions represented with regional features, which could contribute to
575 reduction of forecast errors, especially for precipitation. Therefore, EARR has its own
576 advantage of representing regional features of precipitation better than relatively coarse-
577 resolution global reanalysis.

578

579 **Author contribution**

580 Hyun Mee Kim proposed the main scientific ideas and Eun-Gyeong Yang contributed the
581 supplementary ideas during the process. Eun-Gyeong Yang developed the reanalysis system
582 and produced the 10-year regional reanalysis data. Eun-Gyeong Yang and Hyun Mee Kim

583 analyzed the simulation results and completed the manuscript. Dae-Hui Kim contributed to
584 analyzing the reanalysis data and to the preparation of software and computing resources for
585 the reanalysis system.

586

587 **Competing interests**

588 The authors declare that they have no competing interests.

589

590 **Acknowledgments**

591 The authors appreciate reviewers for their valuable comments. This study was supported by a
592 National Research Foundation of Korea (NRF) grant funded by the South Korean government
593 (Ministry of Science and ICT) (Grant 2021R1A2C1012572) and the Yonsei Signature Research
594 Cluster Program of 2021 (2021-22-0003). This study was carried out by utilizing the
595 supercomputer system supported by the National Center for Meteorological Supercomputer of
596 Korea Meteorological Administration and Korea Research Environment Open NETWORK
597 (KREONET) provided by the Korea Institute of Science and Technology Information. The
598 authors gratefully acknowledge the late Dr. Fuqing Zhang for collaborations at the earlier
599 stages of this study.

600

601

602 **References**

- 603 Ashrit, R., S. Indira Rani, S. Kumar, S. Karunasagar, T. Arulalan, T. Francis, A. Routray, S. I. Laskar,
604 S. Mahmood, P. Jerney, A. Maycock, R. Renshaw, J. P. George, and E. N. Rajagopal, 2020:
605 IMDAA Regional Reanalysis: Performance Evaluation During Indian Summer Monsoon
606 Season. *Journal of Geophysical Research: Atmospheres*, **125**(2), e2019JD030973.
- 607 Bonavita, M., M. Hamrud, and L. Isaksen, 2015: EnKF and hybrid gain ensemble data assimilation.
608 Part II: EnKF and hybrid gain results. *Monthly Weather Review*, **143**(12), 4865-4882.
- 609 Borsche, M, A. K. Kaiser-Weiss, P. Undén, and F. Kaspar, 2015: Methodologies to characterize
610 uncertainties in regional reanalyses. *Adv. Sci. Res.*, **12**, 207-218.
- 611 Bosilovich, M., 2008: NASA's modern era retrospective-analysis for research and applications:
612 Integrating Earth observations. Earthzine, 26 September 2008. [Available online at
613 www.earthzine.org/2008/09/26/nasas-modern-era-retrospective-analysis/.]
- 614 Bosilovich, M., R. Lucchesi, and M. Suarez, 2015: MERRA-2: File specification. NASA GMAO Office
615 Note 9, 73 pp., <http://gmao.gsfc.nasa.gov/pubs/docs/Bosilovich785.pdf>.
- 616 Bromwich, D. H., A. B. Wilson, L. Bai, Z. Liu, M. Barlage, C. F. Shih, S. Maldonado, K. M. Hines, S.-
617 H. Wang, J. Woollen, B. Kuo, H.-C. Lin, T.-K. Wee, M. C. Serreze, and J. E. Walsh, 2018: The
618 Arctic system reanalysis, version 2. *Bulletin of the American Meteorological Society*, **99**(4),
619 805-828.
- 620 Bromwich, D. H., A. B. Wilson, L. S. Bai, G. W. Moore, and P. Bauer, 2016: A comparison of the
621 regional Arctic System Reanalysis and the global ERA-Interim Reanalysis for the Arctic.
622 *Quarterly Journal of the Royal Meteorological Society*, **142**(695), 644-658.
- 623 Cotton, J., M. Forsythe, F. Warrick, K. Salonen, N. Bormann, and K. Lean, 2016: AMVs in the Tropics:
624 use in NWP, data quality and impact, Joint ECMWF/ESA Workshop on 'Tropical modeling,
625 observations and data assimilation [Available online at <https://www.ecmwf.int/node/16865>]
- 626 Dee, D. P., S. M. Uppala, A. J. Simmons, P. Berrisford, P. Poli, S. Kobayashi, U. Andrae, M. A.
627 Balmaseda, G. Balsamo, P. Bauer, P. Bechtold, A. C. M. Beljaars, L. van de Berg, J. Bidlot, N.
628 Bormann, C. Delsol, R. Dragani, M. Fuentes, A. J. Geer, L. Haimberger, S. B. Healy, H.

629 Hersbach, E. V. Hólm, L. Isaksen, P. Kållberg, M. Köhler, M. Matricardi, A. P. McNally, B. M.
630 Monge-Sanz, J.-J. Morcrette, B.-K. Park, C. Peubey, P. de Rosnay, C. Tavalato, J.-N. Thépaut,
631 and F. Vitart, 2011: The ERA-Interim reanalysis: configuration and performance of the data
632 assimilation system. *Q. J. R. Meteorol. Soc.*, **137**, 553–597. doi: 10.1002/qj.828

633 Ebert, E. E., 2008: Fuzzy verification of high-resolution gridded forecasts: a review and proposed
634 framework. *Meteorological Applications: A journal of forecasting, practical applications,*
635 *training techniques and modelling*, **15**(1), 51-64.

636 Fukui, S., T. Iwasaki, K. Saito, H. Seko, and M. Kunii, 2018: A feasibility study on the high-resolution
637 regional reanalysis over Japan assimilating only conventional observations as an alternative to
638 the dynamical downscaling. *Journal of the Meteorological Society of Japan*. **96**(6), 565-585.

639 Gibson, J. K., P. Kållberg, S. Uppala, A. Nomura, A. Hernandez, E. Serrano, 1997: ERA Description.
640 *ECMWF Re-Analysis Final Report Series*, **1**, 71pp.

641 Grell, G. A., and S. R. Freitas, 2014: A scale and aerosol aware stochastic convective parameterization
642 for weather and air quality modeling. *Atmos. Chem. Phys*, **14**(10), 5233-5250.

643 He, J., F. Zhang, X. Chen, X. Bao, D. Chen, H. M. Kim, H.-W. Lai, L. R. Leung, X. Ma, Z. Meng, T.
644 Ou, Z. Xiao, E.-G. Yang, and K. Yang, 2019: Development and evaluation of an ensemble-based
645 data assimilation system for regional reanalysis over the Tibetan Plateau and surrounding
646 regions, *Journal of Advances in Modeling Earth Systems*, **11**(8), 2503-2522.

647 Hersbach, H., B. Bell, P. Berrisford, S. Hirahara, A. Horányi, J. Muñoz-Sabater, J. Nicolas, C. Peubey,
648 R. Radu, D. Schepers, A. Simmons, C. Soci, S. Abdalla, X. Abellan, G. Balsamo, P. Bechtold,
649 G. Biavati, J. Bidlot, M. Bonavita, G. D. Chiara, P. Dahlgren, D. Dee, M. Diamantakis, R.
650 Dragani, J. Flemming, R. Forbes, M. Fuentes, A. Geer, L. Haimberger, S. Healy, R. J. Hogan, E.
651 Hólm, M. Janisková, S. Keeley, P. Laloyaux, P. Lopez, C. Lupu, G. Radnoti, P. de Rosnay, I.
652 Rozum, F. Vamborg, S. Villaume, and J.-N. Thépaut, 2020: The ERA5 global reanalysis.
653 *Quarterly Journal of the Royal Meteorological Society*, **146**(730), 1999-2049.

654 Hersbach, H., P. de Rosnay, B. Bell, D. Schepers, A. Simmons, C. Soci, S. Abdalla, M. Alonso
655 Balmaseda, G. Balsamo, P. Bechtold, P. Berrisford, J. Bidlot, Eric. de Boissésou, M. Bonavita,

656 P. Browne, R. Buizza, P. Dahlgren, D. Dee, R. Dragani, M. Diamantakis, J. Flemming, R. Forbes,
657 A. Geer, T. Haiden, E. Hólm, L. Haimberger, R. Hogan, A. Horányi, M. Janisková, P. Laloyaux,
658 P. Lopez, J. Muñoz-Sabater, C. Peubey, R. Radu, D. Richardson, J.-N. Thépaut, F. Vitart, X.
659 Yang, E. Zsótér, and H. Zuo, 2018: Operational global reanalysis: progress, future directions
660 and synergies with NWP, *ECMWF ERA report series*, N27.

661 Hong, S.-Y., Y. Noh, and J. Dudhia, 2006: A new vertical diffusion package with an explicit treatment
662 of entrainment processes. *Monthly Weather Review*, **134**(9), 2318-2341.

663 Houtekamer, P. L., and F. Zhang, 2016: Review of the ensemble Kalman filter for atmospheric data
664 assimilation. *Monthly Weather Review*, **144**(12), 4489-4532.

665 Iacono, M. J., J. S. Delamere, E. J. Mlawer, M. W. Shephard, S. A. Clough, and W. D. Collins, 2008:
666 Radiative forcing by long-lived greenhouse gases: Calculations with the AER radiative transfer
667 models. *Journal of Geophysical Research: Atmospheres*, **113**(D13).

668 Jerney, P. M., and R. J. Renshaw, 2016: Precipitation representation over a two-year period in regional
669 reanalysis. *Q. J. R. Meteorol. Soc.*, **142**, 1300-1310.

670 Jiménez, P. A., J. Dudhia, J. F. González-Rouco, J. Navarro, J. P. Montávez, and E. García-Bustamante,
671 2012: A revised scheme for the WRF surface layer formulation. *Mon. Wea. Rev.*, **140**(3), 898-
672 918.

673 Kayaba, N., T. Yamada, S. Hayashi, K. Onogi, S. Kobayashi, K. Yoshimoto, K. Kamiguchi, and K.
674 Yamashita, 2016: Dynamical regional downscaling using the JRA-55 reanalysis (DSJRA-55).
675 *Sola*, **12**, pp.1-5.

676 Kalnay, E., M. Kanamitsu, R. Kistler, W. Collins, D. Deaven, L. Gandin, M. Iredell, S. Saha, G. White,
677 J. Woolen, Y. Zhu, M. Chelliah, W. Ebisuzaki, W. Higgins, J. Janowiak, K. C. Mo, C. Ropelewski,
678 J. Wang, A. Leetmaa, R. Reynolds, Roy Jenne and Dennis Joseph, 1996: The NCEP/NCAR 40-
679 year reanalysis project. *Bull. Amer. Meteorol. Soc.*, **77**, 437-471.

680 Kanamitsu, M., W. Ebisuzaki, J. Woollen, S.-K. Yang, J. J. Hnilo, M. Fiorino, and G. L. Potter, 2002:
681 NCEP–DOE AMIP-II Reanalysis (R-2). *Bull. Amer. Meteor. Soc.*, **83**, 1631–1643.

682 Kay, J. K., H. M. Kim, Y.-Y. Park, and J. Son, 2013: Effect of doubling ensemble size on the

683 performance of ensemble prediction in warm season using MOGREPS implemented in
684 KMA, *Advances in Atmospheric Sciences*, **30**(5), 1287-1302, doi:10.1007/s00376-012-2083-y.

685 Keyser, D., 2013: An Overview of Observational Data Processing at NCEP (with information on BUFR
686 Format including “PrepBUFR” files), *GSI tutorial*, August 6, 2013.

687 Kim, S., H. M. Kim, J. K. Kay, and S.-W. Lee, 2015: Development and evaluation of high resolution
688 limited area ensemble prediction system in KMA, *Atmosphere*, 25(1), 67-83. (in Korean with
689 English abstract)

690 Kim, S., and H. M. Kim, 2017: Effect of considering sub-grid scale uncertainties on the forecasts of a
691 high-resolution limited area ensemble prediction system, *Pure and Applied Geophysics*, **174**(5),
692 2021-2037, doi: 10.1007/s00024-017-1513-2.

693 Kistler, R., W. Collins, S. Saha, G. White, J. Woollen, E. Kalnay, M. Chelliah, W. Ebisuzaki, M.
694 Kanamitsu, V. Kousky, H. v. d. Dool, R. Jenne, and M. Fiorino, 2001: The NCEP–NCAR 50–
695 Year Reanalysis: Monthly Means CD–ROM and Documentation. *Bull. Amer. Meteor. Soc.*, **82**,
696 247–267.

697 Kobayashi, S., Y. Ota, Y. Harada, A. Ebita, M. Moriya, H. Onoda, K. Onogi, H. Kamahori, C. Kobayashi,
698 H. Endo, K. Miyaoka, and K. Takahashi, 2015: The JRA-55 reanalysis: General specifications
699 and basic characteristics, *J. Meteorol. Soc. Jpn.*, **93**, 5-48.

700 Mesinger, F., G. DiMego, E. Kalnay, K. Mitchell, P. C. Shafran, W. Ebisuzaki, D. Jović, J. Woollen, E.
701 Rogers, E. H. Berbery, M. B. Ek, Y. Fan, R. Grumbine, W. Higgins, H. Li, Y. Lin, G. Manikin,
702 D. Parrish, and W. Shi, 2006: North American Regional Reanalysis. *Bull. Amer. Meteor. Soc.*,
703 **87**, 343–360.

704 Mittermaier, M. P., 2014: A strategy for verifying near-convection-resolving model forecasts at
705 observing sites. *Weather and Forecasting*, **29**(2), 185-204.

706 National Centers for Environmental Prediction/National Weather Service/NOAA/U.S. Department of
707 Commerce, 2008: NCEP ADP Global Upper Air and Surface Weather Observations
708 (PREPBUFR format). *Research Data Archive at the National Center for Atmospheric Research*,
709 *Computational and Information Systems Laboratory*, Boulder, CO. [Available online at

710 <https://doi.org/10.5065/Z83F-N512>.] Accessed 5 July 2018.

711 National Climatic Data Center/NESDIS/NOAA/U.S. Department of Commerce, Meteorology
712 Department/Florida State University, Climate Analysis Section/Climate and Global Dynamics
713 Division/National Center for Atmospheric Research/University Corporation for Atmospheric
714 Research, and Harvard College Observatory/Harvard University, 1981: World Monthly Surface
715 Station Climatology. *Research Data Archive at the National Center for Atmospheric Research,*
716 *Computational and Information Systems Laboratory*, Boulder, CO. [Available online at
717 <http://rda.ucar.edu/datasets/ds570.0/>.] Accessed 7 Nov 2019.

718 On, N., H. M. Kim, and S. Kim, 2018: Effects of resolution, cumulus parameterization scheme,
719 and probability forecasting on precipitation forecasts in a high-resolution limited-area
720 ensemble prediction system, *Asia-Pacific Journal of Atmospheric Sciences*, **54**, 623-
721 637, doi:10.1007/s13143-018-0081-4.

722 Onogi, K., J. Tsutsui, H. Koide, M. Sakamoto, S. Kobayashi, H. Hatsushika, T. Matsumoto, N.
723 Yamazaki, H. Kamahori, K. Takahashi, S. Kadokura, K. Wada, K. Kato, R. Oyama, T.
724 Ose, N. Mannoji, and R. Taira, 2007: The JRA-25 reanalysis. *J. Meteor. Soc. Japan*, **85**,
725 369–432.

726 Park, J., and H. M. Kim, 2020: Design and evaluation of CO₂ observation network to optimize surface
727 CO₂ fluxes in Asia using observation system simulation experiments, *Atmospheric Chemistry*
728 *and Physics*, **20**, 5175-5195, <https://doi.org/10.5194/acp-20-5175-2020>.

729 Penny, S. G., 2014: The hybrid local ensemble transform Kalman filter. *Monthly Weather Review*,
730 **142**(6), 2139-2149.

731 Penny, S. G., D. W. Behringer, J. A. Carton, and E. Kalnay, 2015: A hybrid global ocean data
732 assimilation system at NCEP. *Monthly Weather Review*, **143**(11), 4660-4677.

733 Que, L. J., W. L. Que, and J. M. Feng, 2016: Intercomparison of different physics schemes in the WRF
734 model over the Asian summer monsoon region. *Atmospheric and Oceanic Science Letters*, **9**(3),
735 169-177.

736 Renshaw, R., P. Jermey, D. Barker, A. Maycock, and S. Oxley, 2013: EURO4M regional reanalysis
737 system, *Forecasting Research Technical Report*, No. **583**, Met Office.

738 Rienecker, M. M., M. J. Suarez, R. Gelaro, R. Todling, J. Bacmeister, E. Liu, M. G. Bosilovich, S. D.
739 Schubert, L. Takacs, G.-K. Kim, S. Bloom, J. Chen, D. Collins, A. Conaty, A. da Silva, W. Gu,
740 J. Joiner, R. D. Koster, R. Lucchesi, A. Molod, T. Owens, S. Pawson, P. Pegion, C. R. Redder,
741 R. Reichle, F. R. Robertson, A. G. Ruddick, M. Sienkiewicz, and J. Woollen, 2011: MERRA:
742 NASA's Modern-Era Retrospective Analysis for Research and Applications. *J. Climate*, **24**,
743 3624–3648.

744 Saha, S., S. Moorthi, H.-L. Pan, X. Wu, J. Wang, S. Nadiga, P. Tripp, R. Kistler, J. Woollen, D. Behringer,
745 H. Liu, D. Stokes, R. Grumbine, G. Gayno, J. Wang, Y.-T. Hou, H.-Y. Chuang, H.-M. H. Juang,
746 J. Sela, M. Iredell, R. Treadon, D. Kleist, P. V. Delst, D. Keyser, J. Derber, M. Ek, J. Meng, H.
747 Wei, R. Yang, S. Lord, H. V. D. Dool, A. Kumar, W. Wang, C. Long, M. Chelliah, Y. Xue, B.
748 Huang, J.-K. Schemm, W. Ebisuzaki, R. Lin, P. Xie, M. Chen, S. Zhou, W. Higgins, C.-Z. Zou,
749 Q. Liu, Y. Chen, Y. Han, L. Cucurull, R. W. Reynolds, G. Rutledge, and M. Goldberg, 2010: The
750 NCEP Climate Forecast System Reanalysis. *Bull. Amer. Meteor. Soc.*, **91**, 1015–1057.

751 Schubert, S., J. Pfendtner, and R. Rood, 1993: An assimilated dataset for earth science applications.
752 *Bull. Amer. Meteor. Soc.*, **74**, 2331–2342.

753 Shiferaw, A., T. Tadesse, C. Rowe, and R. Oglesby, 2018: Precipitation extremes in dynamically
754 downscaled climate scenarios over the greater horn of Africa. *Atmosphere*, **9**(3), 112.

755 Shin, I.-C, J.-G. Kim, C.-Y. Chung, S.-K. Baek, and J.-R. Lee, 2016: The impact of the COMS data on
756 the KMA NWP System, *14th JCSDA Technical Review Meeting & Science Workshop on*
757 *Satellite Data Assimilation*.

758 Skamarock, W. C., J. B. Klemp, J. Dudhia, D. O. Gill, D. M. Barker, M. G. Duda, X.-Y. Huang, W.
759 Wang, J. G. Powers, 2008: A description of the advanced research WRF version 3. NCAR Tech.
760 Note NCAR/TN-475+ STR Available at:
761 <https://opensky.ucar.edu/islandora/object/technotes%3A500/datastream/PDF/view>.

762 Tewari, M., F. Chen, W. Wang, J. Dudhia, M. A. LeMone, K. Mitchell, M. Ek, G. Gayno, J. Wegiel, and

763 R. H. Cuenca, 2004: Implementation and verification of the unified NOAA land surface model
764 in the WRF model. *20th conference on weather analysis and forecasting/16th conference on*
765 *numerical weather prediction* (Vol. 1115). Seattle, WA: American Meteorological Society.

766 Theis, S. E., A. Hense, and U. Damrath, 2005: Probabilistic precipitation forecasts from a deterministic
767 model: A pragmatic approach. *Meteorological Applications: A journal of forecasting, practical*
768 *applications, training techniques and modelling*, **12**(3), 257-268.

769 Thompson, G., P. R. Field, R. M. Rasmussen, and W. D. Hall, 2008: Explicit forecasts of winter
770 precipitation using an improved bulk microphysics scheme. Part II: Implementation of a new
771 snow parameterization. *Mon. Wea. Rev.*, **136**(12), 5095-5115.

772 Uppala, S. M., P. W. KÅllberg, A. J. Simmons, U. Andrae, V. D. C. Bechtold, M. Fiorino, J. K. Gibson,
773 J. Haseler, A. Hernandez, G. A. Kelly, X. Li, K. Onogi, S. Saarinen, N. Sokka, R. P. Allan, E.
774 Andersson, K. Arpe, M. A. Balmaseda, A. C. M. Beljaars, L. V. D. Berg, J. Bidlot, N. Bormann,
775 S. Caires, F. Chevallier, A. Dethof, M. Dragosavac, M. Fisher, M. Fuentes, S. Hagemann, E.
776 Hólm, B. J. Hoskins, L. Isaksen, P. A. E. M. Janssen, R. Jenne, A. P. McNally, J.-F. Mahfouf, J.-
777 J. Morcrette, N. A. Rayner, R. W. Saunders, P. Simon, A. Sterl, K. E. Trenberth, A. Untch, D.
778 Vasiljevic, P. Viterbo, and J. Woollen, 2005: The ERA-40 re-analysis. *Q. J. R. Meteorol. Soc.*,
779 **131**: 2961–3012.

780 Warrick, F., 2015: Options for filling the LEO-GEO AMV Coverage Gap. *NWP SAF Tech. Doc.*, NWP
781 SAF-MO-TR-030, 21 p.

782 Wilks, D. S., 2006: Statistical methods in the atmospheric sciences, 2nd edn., *Academic Press*, 627pp.

783 Wilson, L., 2010: Verification of severe weather forecasts in support of the “SWFDP Southern Africa”
784 project. *Report for the World Meteorological Organisation*, pp. 21
785 (www.wmo.int/pages/prog/www/BAS/documents/Doc-7-Verification.doc)

786 Yang, E.-G., and H. M. Kim, 2017: Evaluation of a regional reanalysis and ERA-Interim over East Asia
787 using in situ observations during 2013-14, *Journal of Applied Meteorology and*
788 *Climatology*, **56**(10), 2821-2844,

789 Yang, E.-G., and H. M. Kim, 2019: Evaluation of Short-Range Precipitation Reforecasts from East Asia

790 Regional Reanalysis. *Journal of Hydrometeorology*, **20**(2), 319-337.

791 Yang, E.-G., and H. M. Kim, 2021a: A comparison of variational, ensemble-based, and hybrid data
792 assimilation methods over East Asia for two one-month periods, *Atmospheric Research*, **249**,
793 105257.

794 Yang, E.-G., and H. M. Kim, 2021b: East Asia Regional Reanalysis 6 hourly data on pressure levels
795 from 2010 to 2019, <https://doi.org/10.7910/DVN/7P8MZT>, Harvard Dataverse, V1.

796 Yang, E.-G., and H. M. Kim, 2021c: East Asia Regional Reanalysis 6 hourly precipitation data from
797 2010 to 2019, <https://doi.org/10.7910/DVN/Q07VRC>, Harvard Dataverse, V1.

798 Yoo, C., and E. Cho, 2018: Comparison of GCM precipitation predictions with their RMSEs and pattern
799 correlation coefficients. *Water*, **10**(1), 28.

800 Zhang, F., M. Zhang, and J. Poterjoy, 2013: E3DVar: Coupling an ensemble Kalman filter with three-
801 dimensional variational data assimilation in a limited-area weather prediction model and
802 comparison to E4DVar. *Monthly Weather Review*, **141**(3), 900-917.

803 Zhang, Q., Y. Pan, S. Wang, J. Xu, and J. Tang, 2017: High-resolution regional reanalysis in China:
804 Evaluation of 1 year period experiments. *Journal of Geophysical Research: Atmospheres*,
805 **122**(20), 10-801.

806

807 **Table caption**

808 Table 1. Model configuration.

809 Table 2. Summary of observations used in this study. The default observation error statistics
810 provided in WRFDA system are used for assimilation in this study. The variables u , v , T , RH ,
811 P_s , and TPW denote zonal wind, meridional wind, temperature, relative humidity, surface
812 pressure, and total precipitable water, respectively.

813 Table 3. (Re)analyses and (re)forecasts and corresponding experiments used in this study.

814 Table 4. The 2×2 contingency table for dichotomous (yes-no) events.

815

816 **Figure caption**

817 Figure 1. The East Asia Regional Reanalysis domain. The black dashed box denotes a
818 verification area. Different types of NCEP PrepBUFR observations are available for
819 assimilation at 00 UTC on 1st of January in 2017.

820 Figure 2. The schematic diagram of the advanced hybrid gain data assimilation method in the
821 East Asia regional reanalysis system.

822 Figure 3. RMSEs of analysis of (a,b) zonal wind, (c,d) meridional wind, (e,f) temperature, and
823 (g,h) Qvapor (water vapor mixing ratio) from ERA-I (black dashed), ERA5 (black solid),
824 E3DVAR (blue dashed), AdvHG (blue solid) depending on pressure levels for (left) January
825 and (right) July in 2017.

826 Figure 4. Same as Fig. 3 except for 24 h forecast.

827 Figure 5. Same as Fig. 3 except for 36 h forecast.

828 Figure 6. RMSEs of analysis of (a) zonal wind, (b) meridional wind, (c) temperature, and (d)
829 Qvapor (water vapor mixing ratio) from ERA5 (black solid) and AdvHG (blue solid) and
830 spreads of analysis (black dashed) and 6 h forecast (gray dashed) of AdvHG depending on
831 pressure levels averaged over the ten-year period of 2010-2019.

832 Figure 7. Same as Fig. 6 except for RMSE of 24 h forecast.

833 Figure 8. (a,c) ETS and (b,d) FBI for (a,b) January and (c,d) July in 2017 depending on
834 thresholds 0.5, 1, 4, 8, and 16 mm (6 h)⁻¹.

835 Figure 9. (a,c) POD and (b,d) FAR for (a,b) January and (c,d) July in 2017 depending on
836 thresholds 0.5, 1, 4, 8, and 16 mm (6 h)⁻¹.

837 Figure 10. Brier skill score of the probabilistic postprocessed forecast with reference to the

838 WRF-based ERA-I for (a-d) January and (e-h) July in 2017 (Blue solid: AdvHG, blue dashed:
839 E3DVAR, red solid: WRF-based ERA5).

840 Figure 11. The spatial distribution of 6 h accumulated precipitation of (1st column) observation,
841 (2nd column) E3DVAR, (3rd column) AdvHG, (4th column) ERA-I, (5th column) ERA5, (6th
842 column) ERA-I_fromECMWF, and (7th column) ERA5_fromECMWF and the pattern
843 correlation coefficient (PCC) shown at the bottom right of each figure at valid time (1st low, 3rd
844 low) 06 UTC and (2nd low, 4th low) 18 UTC on 29th and 30th of January in 2017.

845 Figure 12. As in Fig. 11, but for 1st and 2nd of July in 2017.

846 Figure 13. The spatial distribution of the monthly accumulated precipitation of (a) observations,
847 (b) E3DVAR, (c) AdvHG, (d) ERA-I, (e) ERA5, (f) ERA-I from ECMWF, and (g) ERA5 from
848 ECMWF for January 2017.

849 Figure 14. As in Fig. 13, but for July 2017.

850

851 Table 1. Model configuration

	Description
Hori. Resol.	12 km (540×432 grid points)
Vert. Lev.	50 vertical levels (up to 5 hPa)
Model	WRF Model (v3.7.1, Skamarock et al. 2008)
LBC	ERA5 (Hersbach et al. 2020)
Data assimilation	E3DVAR (Zhang et al. 2013), Adanced hybrid gain method
Microphysics	Thompson scheme (Thompson et al. 2008)
Cumulus convection	Grell–Freitas ensemble scheme (Grell and Freitas 2014)
PBL	Yonsei University scheme (Hong et al. 2006)
Radiation	Rapid Radiative Transfer Model (RRTMG) scheme (Iacono et al. 2008)
Surface layer	Revised MM5 Monin-Obukhov scheme (Jiménez et al. 2012)
Surface model	Unified Noah Land Surface Model (Tewari et al. 2004)

852

853

854 Table 2. Summary of observations used in this study. The default observation error statistics
 855 provided in WRFDA system are used for assimilation in this study. The variables u, v, T, RH,
 856 Ps, and TPW denote zonal wind, meridional wind, temperature, relative humidity, surface
 857 pressure, and total precipitable water, respectively.

Observations	Descriptions	Variables	Observation errors (depending on vertical levels)
SOUND	Upper-air observation from radiosonde	u, v	1.1-3.3 m/s
		T	1 K
		RH	10-15%
PROFILER	Upper-air wind profile from wind profiler	u, v	2.2-3.2 m/s
PILOT	Upper-air wind profile from pilot balloon or radiosonde	u, v	2.2-3.2 m/s
AIREP	Upper-air wind and temperature from aircraft	u, v	3.6 m/s
		T	1 K
Scatwind	Scatterometer oceanic surface winds	u, v	2.5-3.8 m/s
SHIPS	Surface synoptic observation from ship	u, v	1.1 m/s
		T	2 K
		Ps	1.6 hPa
		RH	10%
SYNOP	Surface synoptic observation from land station	u, v	1.1 m/s
		T	2 K
		Ps	1 hPa
		RH	10%
BUOY	Surface synoptic observation from buoy	u, v	1.4-1.6 m/s
		T	2 K
		Ps	0.9-1 hPa
		RH	10%
GPSPW	Precipitable water vapor from global positioning system (GPS)	TPW	0.2 mm
METAR	Aviation routine weather report from automatic weather station (AWS)	u, v	1.1 m/s
		T	2 K
		Ps	1 hPa
		RH	10%
AMV	Conventional atmospheric motion vector data from satellites	u, v	2.5-4.5 m/s

858

859

860

861 Table 3. (Re)analyses and (re)forecasts and corresponding experiments used in this study.

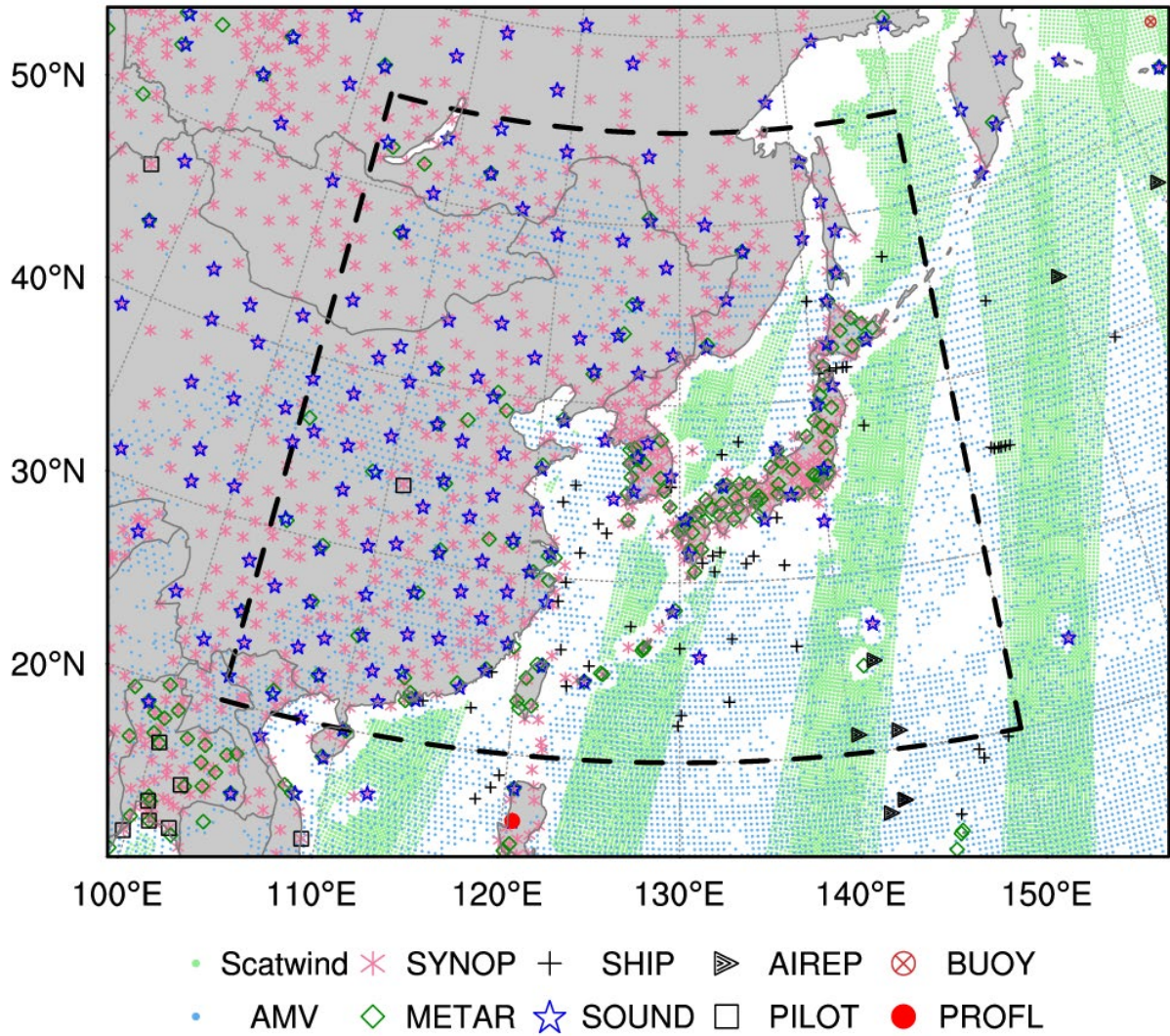
Experiment	(Re)analysis (initial condition)	(Re)forecast	(Re)forecast horizontal resolution (km)	Initial time	Boundary condition in WRF
AdvHG (EARR)	Reanalysis from AdvHG	Generated using WRF	12	00/06/ 12/18 UTC	ERA5
E3DVAR	Analysis from E3DVAR	Generated using WRF	12		
WRF-based ERA5	Reanalysis from ERA5	Generated using WRF	12		
WRF-based ERA-I	Reanalysis from ERA-I	Generated using WRF	12		
ERA5_fromECMWF	Reanalysis from ERA5	Downloaded from ECMWF	31		N/A
ERA-I_fromECMWF	Reanalysis from ERA-I	Downloaded from ECMWF	79		

862

863 Table 4. The 2×2 contingency table for dichotomous (yes-no) events.

Forecast	Observed		
	Yes	No	
Yes	Hits (A)	False alarms (B)	A + B
No	Misses (C)	Correct rejections (D)	C + D
	A + C	B + D	Total = A + B + C + D

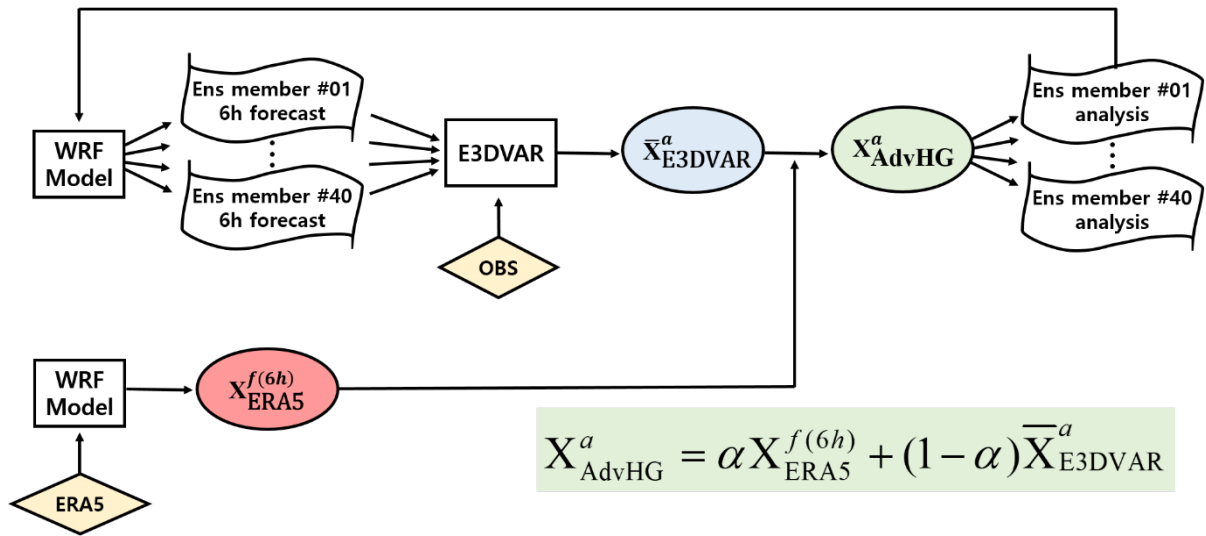
864



865

866 Figure 1. The East Asia Regional Reanalysis domain. The black dashed box denotes a
 867 verification area. Different types of NCEP PrepBUFR observations are available for
 868 assimilation at 00 UTC on 1st of January in 2017.

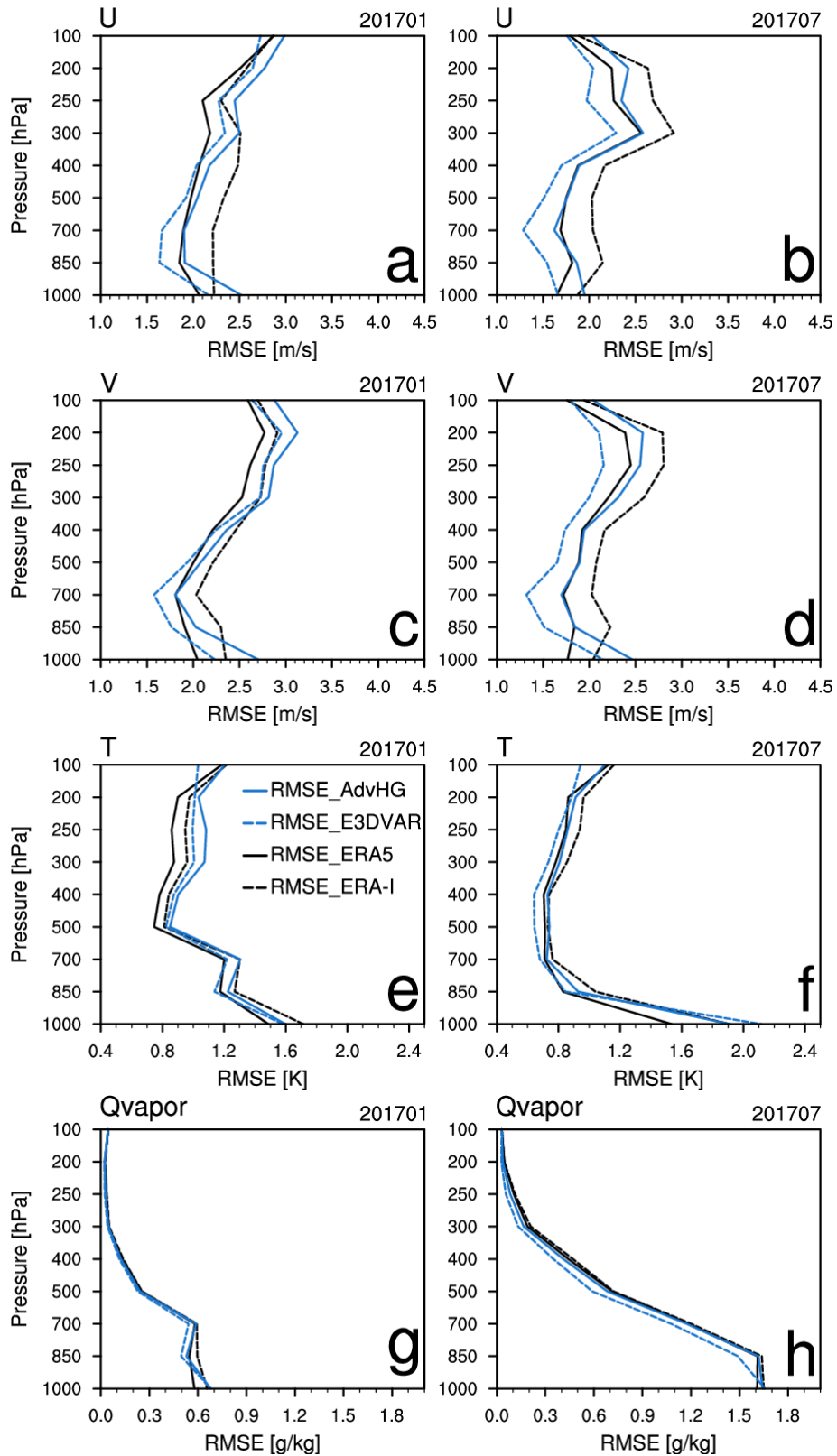
869



870

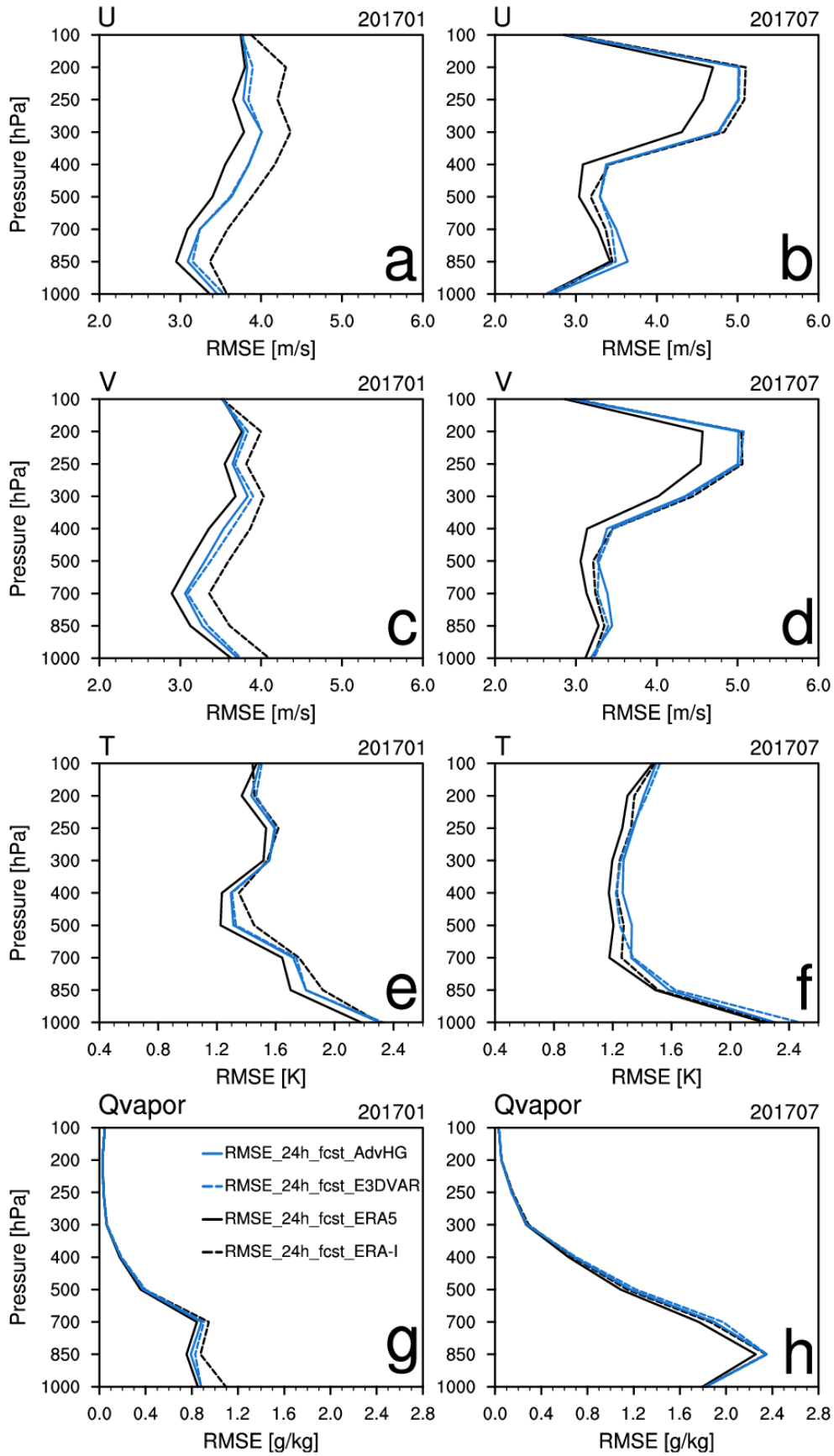
871 Figure 2. The schematic diagram of the advanced hybrid gain data assimilation method in the
 872 East Asia regional reanalysis system.

873



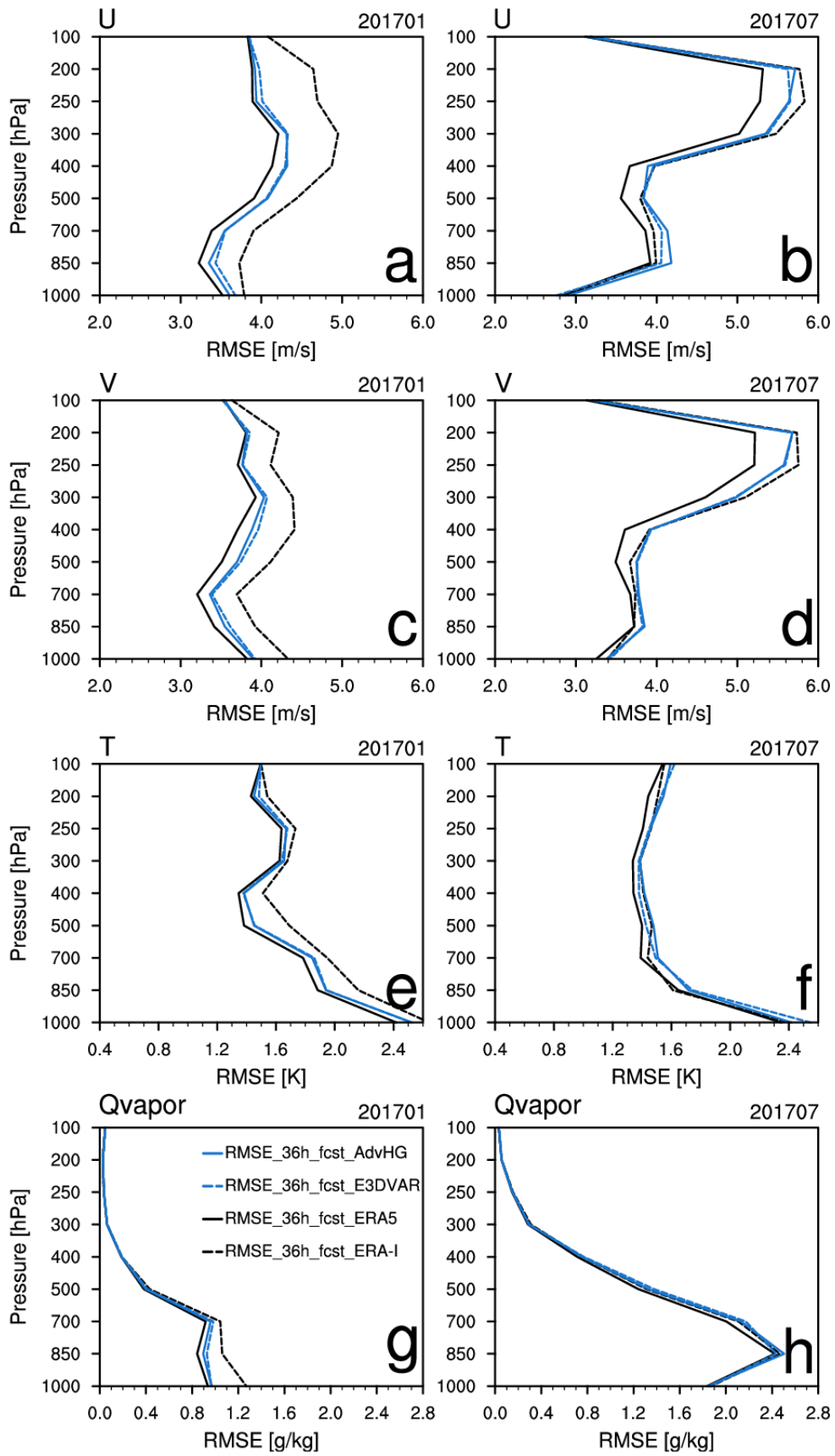
874

875 Figure 3. RMSEs of analysis of (a,b) zonal wind, (c,d) meridional wind, (e,f) temperature, and
 876 (g,h) Qvapor (water vapor mixing ratio) from ERA-I (black dashed), ERA5 (black solid),
 877 E3DVAR (blue dashed), AdvHG (blue solid) depending on pressure levels for (left) January
 878 and (right) July in 2017.



879

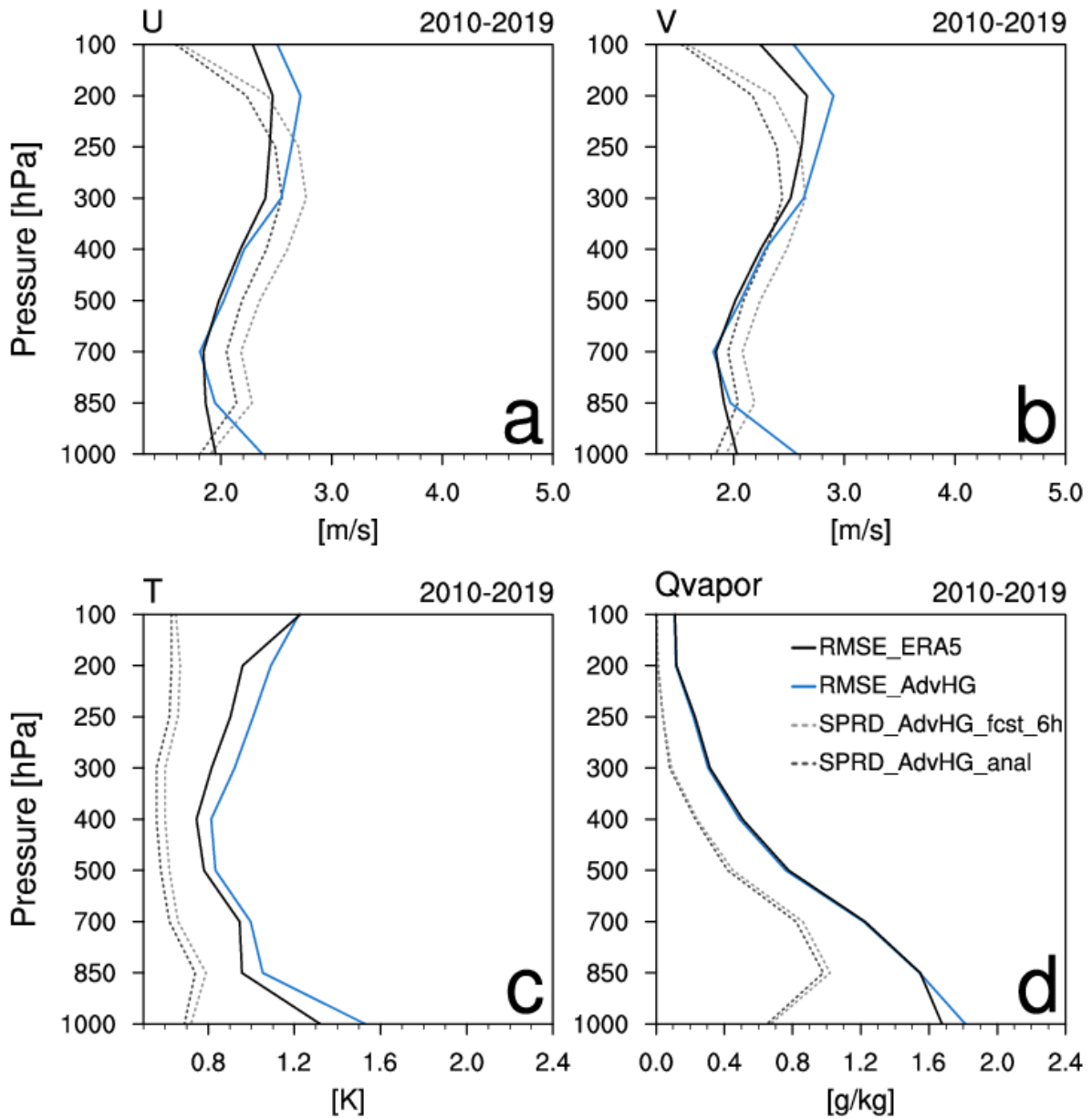
880 Figure 4. Same as Fig. 3 except for 24 h forecast.



881

882 Figure 5. Same as Fig. 3 except for 36 h forecast.

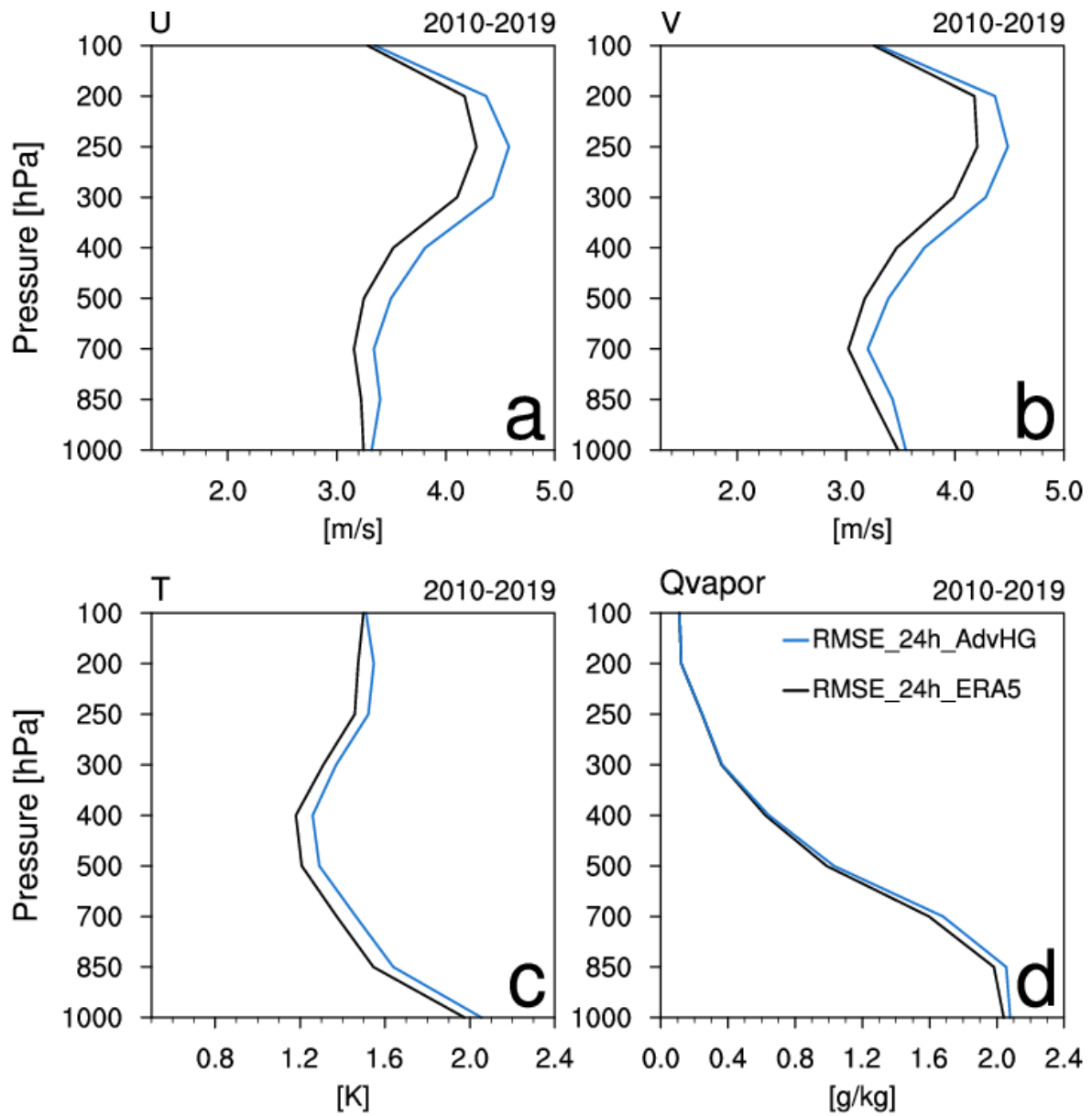
883



884

885 Figure 6. RMSEs of analysis of (a) zonal wind, (b) meridional wind, (c) temperature, and (d)
 886 Qvapor (water vapor mixing ratio) from ERA5 (black solid) and AdvHG (blue solid) and
 887 spreads of analysis (black dashed) and 6 h forecast (gray dashed) of AdvHG depending on
 888 pressure levels averaged over the ten-year period of 2010–2019.

889

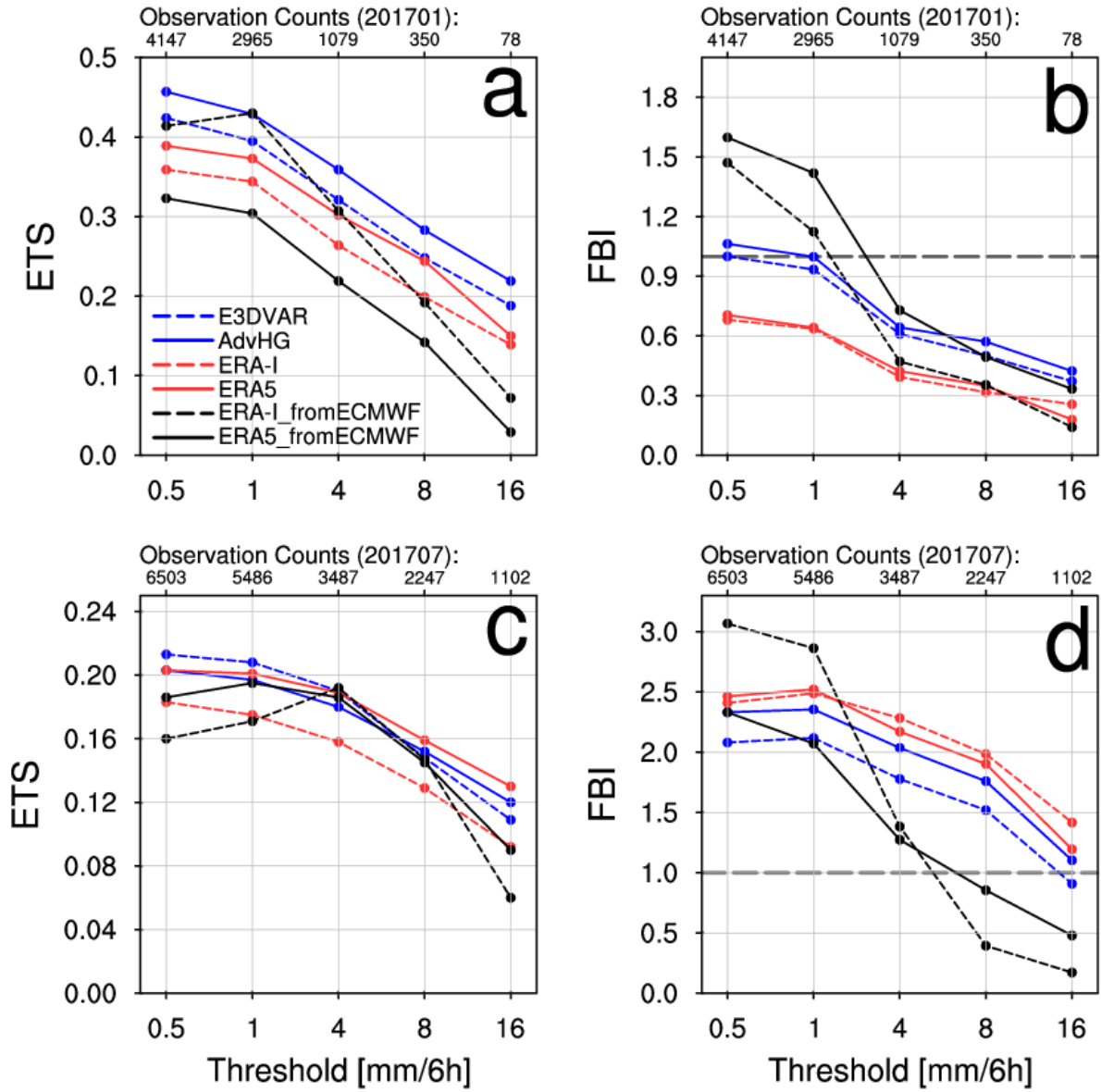


890

891 Figure 7. Same as Fig. 6 except for RMSE of 24 h forecast.

892

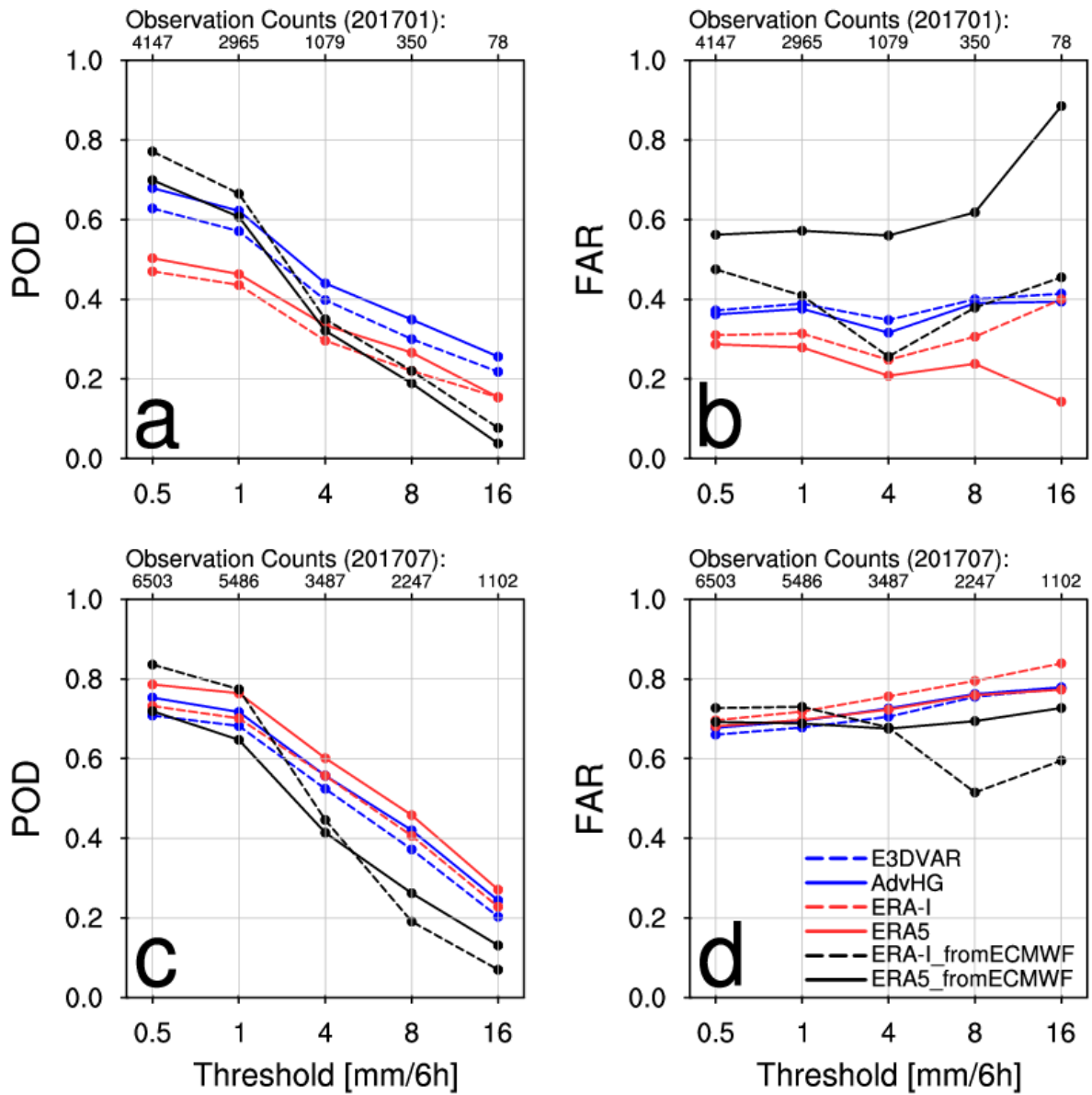
893



894

895 Figure 8. (a,c) ETS and (b,d) FBI for (a,b) January and (c,d) July in 2017 depending on
 896 thresholds 0.5, 1, 4, 8, and 16 mm (6 h)⁻¹.

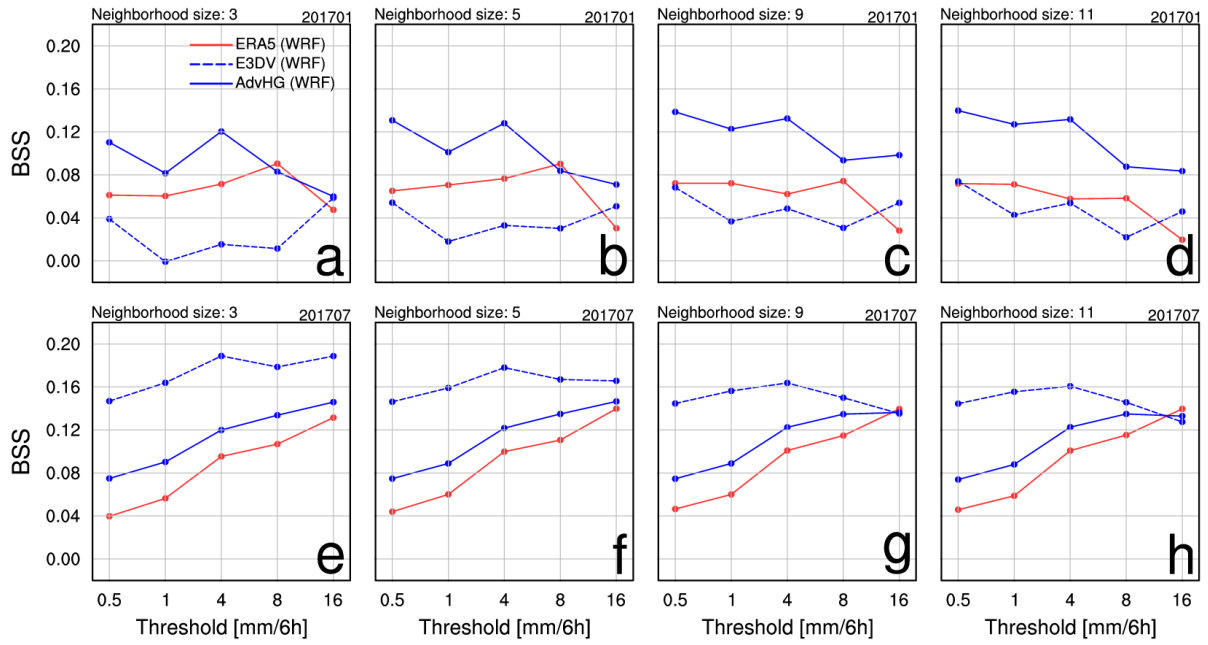
897



898

899 Figure 9. (a,c) POD and (b,d) FAR for (a,b) January and (c,d) July in 2017 depending on
 900 thresholds 0.5, 1, 4, 8, and 16 mm (6 h)⁻¹.

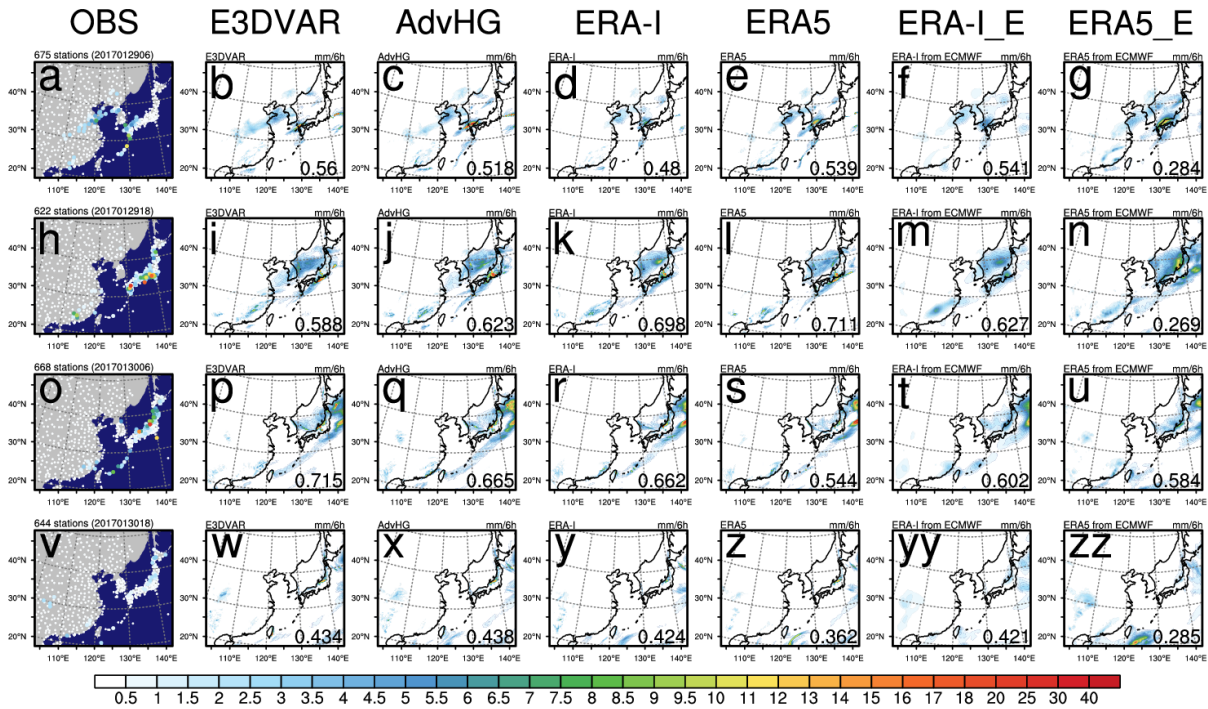
901



902

903 Figure 10. Brier skill score of the probabilistic postprocessed forecast with reference to the
 904 WRF-based ERA-I for (a-d) January and (e-h) July in 2017 (Blue solid: AdvHG, blue dashed:
 905 E3DVAR, red solid: WRF-based ERA5).

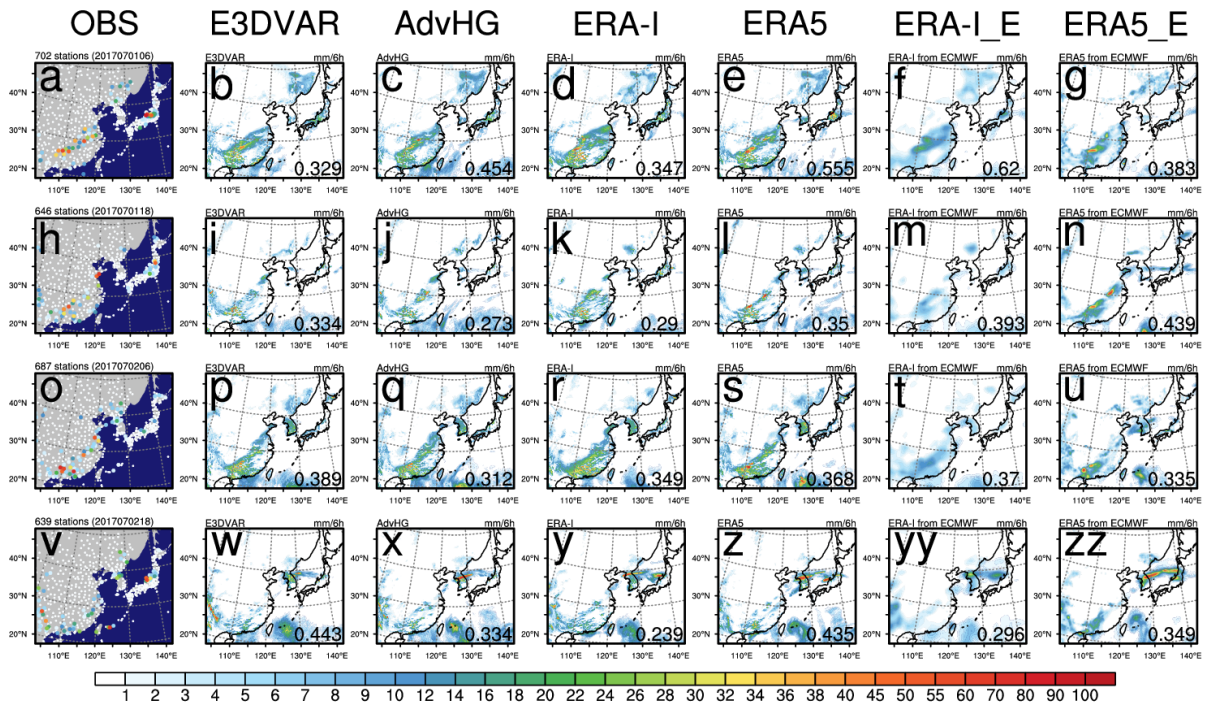
906



907

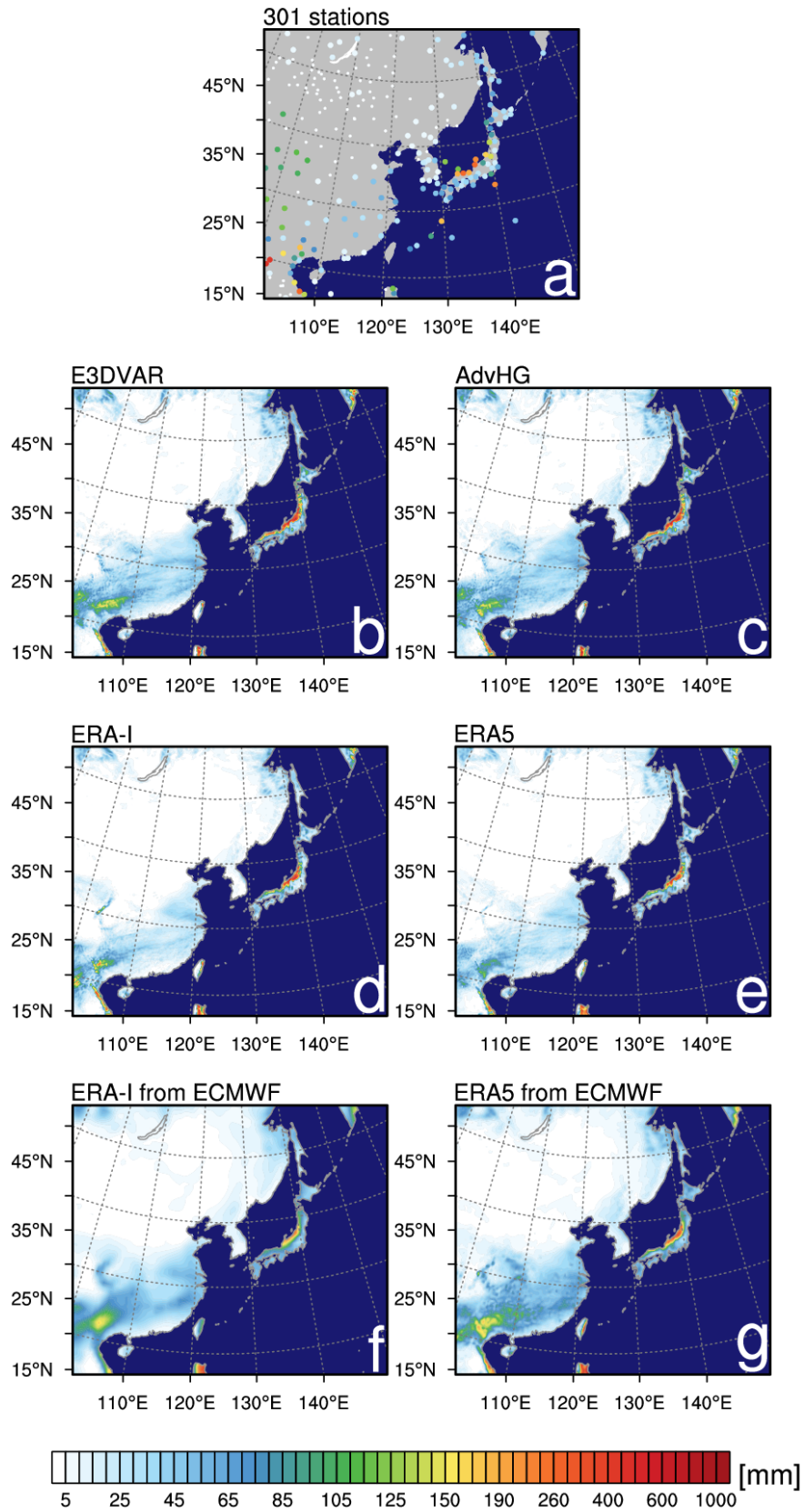
908 Figure 11. The spatial distribution of 6 h accumulated precipitation of (1st column) observation,
 909 (2nd column) E3DVAR, (3rd column) AdvHG, (4th column) ERA-I, (5th column) ERA5, (6th
 910 column) ERA-I_fromECMWF, and (7th column) ERA5_fromECMWF and the pattern
 911 correlation coefficient (PCC) shown at the bottom right of each figure at valid time (1st low, 3rd
 912 low) 06 UTC and (2nd low, 4th low) 18 UTC on 29th and 30th of January in 2017.

913



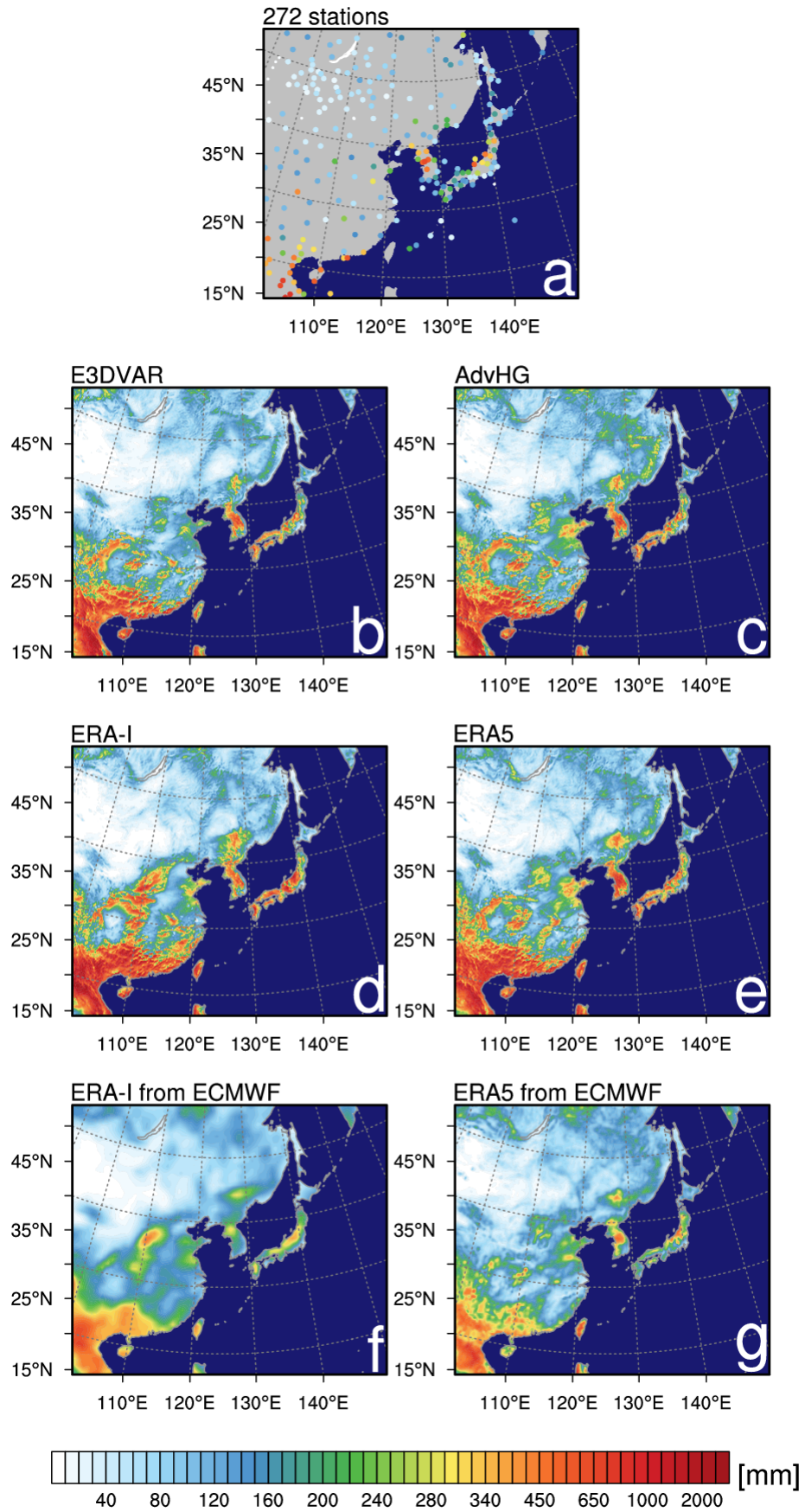
914

915 Figure 12. As in Fig. 11, but for 1st and 2nd of July in 2017.



916

917 Figure 13. The spatial distribution of the monthly accumulated precipitation of (a) observations,
 918 (b) E3DVAR, (c) AdvHG, (d) ERA-I, (e) ERA5, (f) ERA-I from ECMWF, and (g) ERA5 from
 919 ECMWF for January 2017.



920

921 Figure 14. As in Fig. 13, but for July 2017.